Potential Field Artillery Projectile Improvement Using Movable Canards

by Mark F. Costello
U.S. MILITARY ACADEMY

19970505 209

DTIC QUALITY INSPECTED 1

Army Research Laboratory

Aberdeen Proving Ground, MD 21005-5066

ARL-TR-1344 | April 1997

Potential Field Artillery Projectile Improvement Using Movable Canards

Mark F. Costello
U.S. Military Academy

Abstract

This report explores the possibility of actively controlling a projectile with four canard lifting surfaces, equally spaced radially, with the end goals of extending range, improving terminal accuracy, and shaping the trajectory of a projectile. A description of a general mathematical model used to predict the dynamic behavior of a canard-controlled projectile in atmospheric flight is given. The model is exercised in prediction of the response of an advanced projectile currently under development. For the projectile used in this study, it is shown that the maximum range can be extended by 148% using controlled canards. It is also shown that projectile trajectories can be shaped to follow a predetermined and significantly different path than the nominal trajectory.

Contents

Intentionally left blank

List of Figures

Intentionally left blank

List of Tables

Intentionally left blank

1   Introduction.

Traditionally, field artillery target effects are produced by firing a sufficient number of rounds with known accuracy at a given target so that, statistically, the target is neutralized. While this methodology is certainly successful for eliminating targets on the battlefield, it is not without several undesirable side effects that degrade overall effectiveness. Unless you are able to increase the lethality of the munitions, the goal of improving field artillery systems generally boils down to increasing achievable range and improving terminal accuracy of the projectile.

It is obvious that a round with extended range enjoys the flexibility of being able to engage a greater number of targets over a larger land area. A less obvious, yet equally important advantage of extended range is that the system with greater range requires fewer repositionings on the battlefield and can provide fire support for a higher percentage of time. This becomes particularly important in today's highly mobile battle environment, where a significant portion of time is spent moving into position. In a highly mobile battle environment, the commander seeks to minimize decision cycle time. That is to say, he is attempting to minimize the time needed to gather information, analyze the data, make a decision, publish the course of action, and execute the plan. The friendly commander's goal is to operate inside the enemy's decision cycle, in other words, to make decisions and execute operations faster than the enemy can react to these operations, thus introducing confusion and disarray into the enemy's actions. Since a long-range projectile can cover a large area of land, rounds can be fired at many different targets on the battlefield in a short period of time. While the enemy is repositioning to react to artillery fire at a particular target, the long range artillery system can quickly engage the repositioned unit or other targets on the battlefield. Thus, a long range projectile adds increased flexibility to the field artillery commander, allowing him to influence a much greater portion of the battlefield, for longer periods of time.

The intensity of Army operations dictates that the field artillery optimize target effects with every round fired. One method of improving target effects is to increase the terminal accuracy of each round [1]. Current field artillery doctrine requires large numbers of rounds to be fired in order to neutralize a particular target. Statistically, only a small percentage of these rounds actually produces effects on the target. Increased accuracy provides that the 'extra' rounds, those not having effects on target, are never fired. If more rounds than necessary are fired, the firing unit accepts an unnecessary risk of being acquired by enemy target acquisition assets and subsequently engaged with counter fire. When the firing unit comes under steady counter fire, the unit will reposition and be rendered unavailable for other missions while in transit. Also, firing more than the minimum number of rounds needed to eliminate a target wastes expensive munitions and burdens the resupply system. Every extra round expended on a particular target represents an opportunity cost that could have been directed at another objective on the battlefield. More importantly, target effects decrease exponentially as a function of the number of projectiles fired at a particular target due to the lack of surprise. The first volley fired is by far the most important volley to achieve maximum target effectiveness. Furthermore, if rounds are inaccurate, targets will reappear on the battlefield. Potentially, this will require additional artillery engagements and negatively affect the outcome of the overall battle plan. Thus, increased terminal accuracy increases target effects by landing more first hits, reduces vulnerability by firing less shots, and uses less material, which reduces the burden on the supply system - all contributing to a more effective and lethal field artillery unit.

Generally, the line between a target and an artillery cannon determines the angle at which a target is engaged. Once positioned, the commander has little ability to effect the angle or direction which a target is attacked. If the commander desires to attack a target from a different direction, the firing unit must be repositioned to an area located on the same line as the desired engagement direction. As a matter of practicality, this is seldom done, since the benefits associated with attacking a target in the optimal line of fire seldom outweigh the disadvantages of taking a firing unit out of action for repositioning. Obviously, some directions are not possible, such as attacking the enemy from behind the enemy's front line. With active control, the trajectory of a projectile can be drastically altered so that targets can be attacked from a wide variety of angles of inclination as well as different directions. An actively controlled projectile allows the field artillery commander to engage difficult targets due to the ability to attack targets from different directions and renders the unit available for missions for a greater percentage of time due to reduced repositioning requirements.

The work presented in this report explores the possibility of actively controlling a projectile with four

canard lifting surfaces, equally spaced radially, with the end goals of extending range, improving terminal accuracy, and tailoring the trajectory of a projectile. The report begins with a description of a generic mathematical model used to predict the dynamic behavior of a canard-controlled projectile in atmospheric flight. Next, the model is exercised in prediction of the response of an advanced projectile currently under development.

2 Projectile Mathematical Modeling.

The following sections describe the equations used to simulate a canard-controlled projectile. It is assumed that the projectile is a rigid body modeled by a fully coupled six-degree-of-freedom nonlinear set of ordinary differential equations. Aerodynamic forces and moments of the projectile body and canard lifting surfaces are functions of both angle of attack and local Mach number. Air density and the local speed of sound are computed using the standard atmosphere modified to allow for variation in the sea level temperature. The control system uses inertial position and velocity, roll rate, and attitude feedback to track an inertial position trajectory using the movable canard lifting surfaces.

2.1 Atmosphere Model

The trajectory of a projectile depends on the density of air in which it is flying. Since air density varies with atmospheric conditions, measurements of the trajectory of a projectile taken during different atmospheric conditions can be compared with one another only after having been reduced to certain standard conditions. For this purpose, a standard atmosphere was developed and is used regularly in the Aerospace community. Expressions for air density, ρ, and speed of sound, a, as a function of altitude, z, are given by Equations 1 and 4, respectively. See Von Mises [2] for a complete development of the standard atmosphere equations.

$$\rho = 0.00237847(1 + 0.00000688z)^{4.258} \qquad \text{if } 0 > z > -35,332 \text{ feet} \tag{1}$$

$$a = 49.0124\sqrt{518.4 + 0.003566z} \tag{2}$$

If $z < -35,332$ feet, then the value of air density at an altitude of $-35,332$ feet is used. Note that projectile altitude is defined as positive downward so that flight above the ground plane results in a negative value of z. One of the assumptions in the standard atmosphere is that air temperature at sea level is $59°$ F. For a nonstandard day, temperature at sea level is given by Equation 3.

$$T_0 = 1.8 \text{ OAT} + 518.4 \tag{3}$$

In Equation 3, OAT is the outside air temperature and is the difference from the standard temperature given in units of Celsius. OAT $= 0$ is the standard day temperature at sea level. Expressions for air density and speed of sound as a function of altitude and outside air temperature can be derived and are given by Equations 4 and 5.

$$\rho = \frac{1.233}{T_0}(1 + \frac{0.00356z}{T_0})^{4.258} \qquad \text{if } 0 > z > -35,332 \text{ feet} \tag{4}$$

$$a = 49.0124\sqrt{T_0 + 0.003566z} \tag{5}$$

The Earth's atmosphere generally fosters air velocity perturbations that can significantly modify the trajectory of a projectile. It is common to separate the atmospheric air velocity perturbations into steady and fluctuating components, typically called mean wind and atmospheric turbulence, respectively. The atmospheric wind velocity model adopted in the current effort includes only a mean wind component and assumes that the atmospheric wind flows parallel to the Earth's surface. The magnitude of the atmospheric mean wind velocity vector, given by Equation 6, is modeled as an arc tangent function in order to account for the Earth's boundary layer. Figure 1 depicts the atmospheric mean wind velocity as a function of altitude with $\sigma = 100$.

$$V_{mw} = \frac{2\sigma}{\pi} \tan^{-1}\left(\frac{|z|}{1000}\right) \tag{6}$$
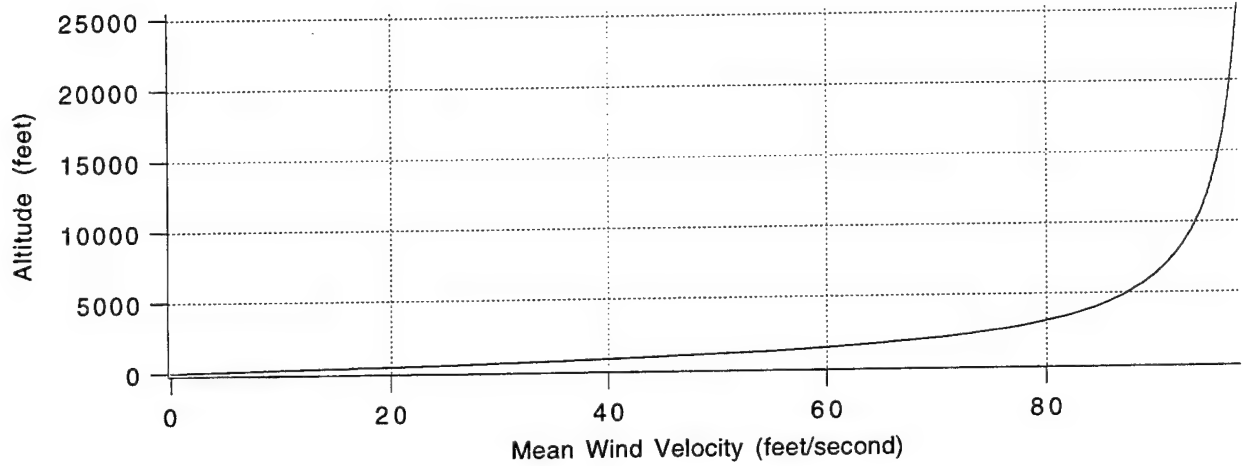
Figure 1: Mean wind velocity versus altitude ($\sigma = 100$).

Because the arc tangent function approaches $\pi/2$ at infinity, Equation 6 approaches σ as altitude increases. The atmospheric mean wind flows over the Earth's surface at an arbitrary angle, ψ_w. A value of $\psi_w = 0°$ implies an initial headwind on the projectile, $\psi_w = 90°$ implies an initial right cross wind, $\psi_w = 180°$ implies an initial tailwind, and $\psi_w = 270°$ implies an initial left cross wind acting on the projectile. Note that the atmospheric mean wind model is quite crude and is merely a simple method for introducing trajectory errors due to atmospheric wind.

2.2 Projectile Dynamic Model.

The motion of a projectile in atmospheric flight is assumed to be adequately described with six rigid body degrees of freedom comprised of three body inertial position coordinates as well as three Euler angle body attitudes. Figure 2 illustrates the inertial and body coordinate systems used in the current effort. The inertial coordinate system, in its most pure form, is fixed or in uniform translation relative to the stars. For the present study, the Earth is presumed to be a flat surface. Thus, the inertial coordinate system is defined as an earth surface fixed coordinate system denoted by subscript I. The inertial system's origin is located at the end of the gun tube with $\vec{\imath}_I$ and $\vec{\jmath}_I$ forming a plane parallel to the Earth's surface. The $\vec{k}_I$ axis points down into the Earth's surface. The projectile body system, denoted with subscript B, is fixed to the center of gravity of the projectile. The $\vec{\imath}_B$ axis points out the nose of the round. If the quadrant elevation angle were zero, then the $\vec{\imath}_B$ and $\vec{\imath}_I$ axes would initially be aligned [3]. Looking down on the projectile with roll angle equal zero, the $\vec{\jmath}_B$ axis points out the right canard wing and $\vec{k}_B$ axis points down. The equations of motion are written with respect to body coordinates with appropriate kinematic equations relating body translational and rotational rates with inertial translational and Euler angle rotational rates, respectively. The resulting 12 nonlinear differential equations are given by Equations 7 through 18. See References [3,4] for a detailed derivation.

$$\dot{x} = u\cos\theta\cos\psi + v(\sin\phi\sin\theta\cos\psi - \cos\phi\sin\psi) + w(\cos\phi\sin\theta\cos\psi + \sin\phi\sin\psi) \tag{7}$$

$$\dot{y} = u\cos\theta\sin\psi + v(\sin\phi\sin\theta\sin\psi + \cos\phi\cos\psi) + w(\cos\phi\sin\theta\sin\psi - \sin\phi\cos\psi) \tag{8}$$

$$\dot{z} = -u\sin\theta + v\sin\phi\cos\theta + w\cos\phi\cos\theta \tag{9}$$

$$\dot{\phi} = p + q\sin\phi\tan\theta + r\cos\phi\tan\theta \tag{10}$$

$$\dot{\theta} = q\cos\phi - r\sin\phi \tag{11}$$

$$\dot{\psi} = q\sin\phi\sec\theta + r\cos\phi\sec\theta \tag{12}$$

3
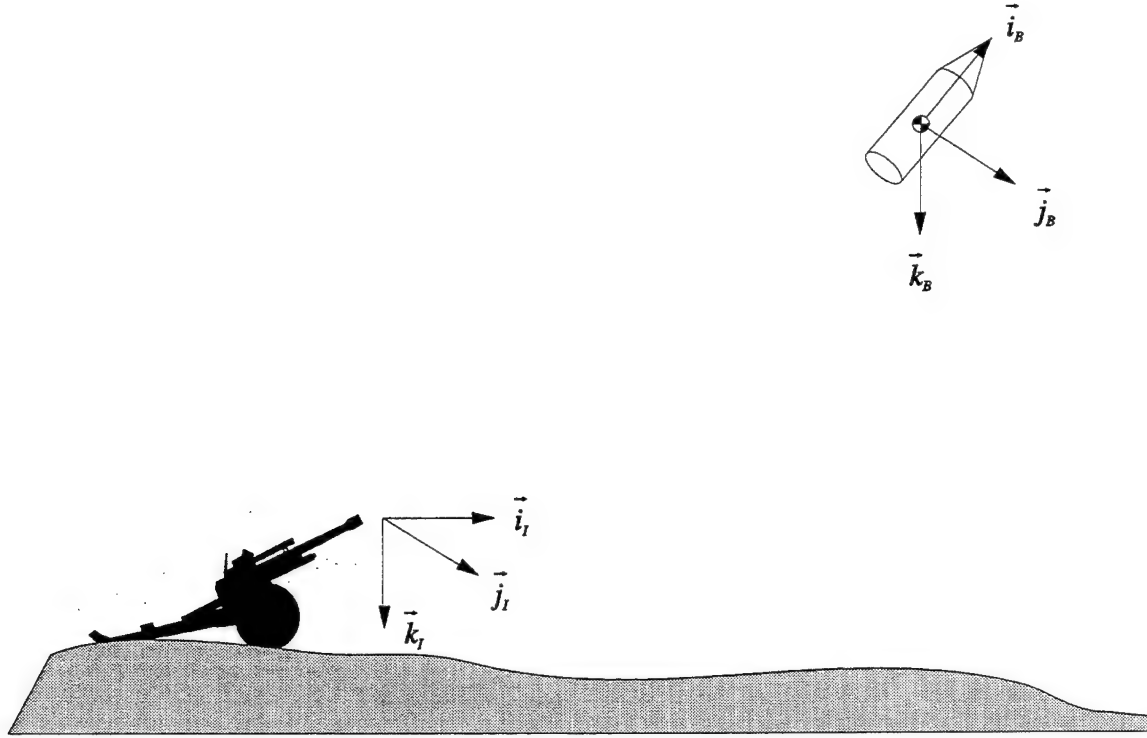
Figure 2: Coordinate system description.

$$\dot{u} = X/m + rv - qw \tag{13}$$

$$\dot{v} = Y/m + pw - ru \tag{14}$$

$$\dot{w} = Z/m + qu - pv \tag{15}$$

$$\dot{p} = L/I_{xx} \tag{16}$$

$$\dot{q} = M/I_{yy} + rp(I_{yy} - I_{xx})/I_{yy} \tag{17}$$

$$\dot{r} = N/I_{yy} + pq(I_{yy} - I_{xx})/I_{yy} \tag{18}$$

Note the following variable definitions utilized in the previous equations: x, y, and z are the measure numbers of the inertial position vector expressed in the inertial reference frame; ϕ is the Euler roll angle, θ is the Euler pitch angle, ψ is the Euler yaw angle; u, v, and w are the translational velocity components of the center of gravity of the projectile resolved in the body axis system; p, q, and r are the components of the angular velocity vector of the projectile with respect to inertial space expressed in the body frame; m is the projectile mass; I_{xx} and I_{yy} are the roll and pitch moments of inertia about the center of gravity, respectively. The applied forces X, Y, and Z and moments L, M, and N are given by Equations 19 through 24.

$$X = -F_p - mg\sin\theta + X_w \tag{19}$$

$$Y = \frac{-v_a}{\sqrt{w_a^2 + v_a^2}} F_n + mg\sin\phi\cos\theta + Y_w \tag{20}$$

$$Z = \frac{-w_a}{\sqrt{w_a^2 + v_a^2}} F_n + mg\cos\phi\cos\theta + Z_w \tag{21}$$

$$L = M_r + L_w \tag{22}$$

$$M = \frac{w_a}{\sqrt{w_a^2 + v_a^2}} M_p + M_w \tag{23}$$

4

Figure 3: Projectile body aerodynamic forces.

$$N = \frac{-v_a}{\sqrt{w_a^2 + v_a^2}} M_p + N_w \tag{24}$$

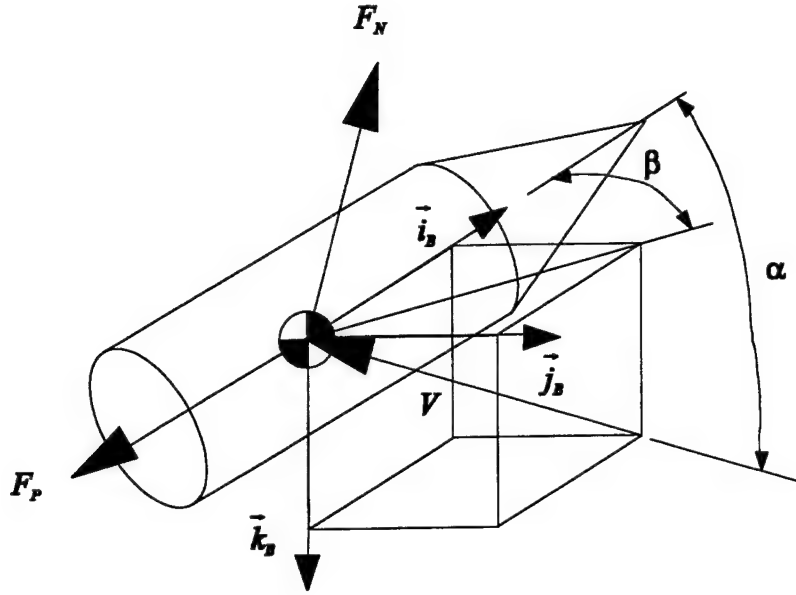Note the following variable definitions used in Equations 19 through 24: F_p and F_n are the drag and normal body aerodynamic forces acting at the projectile center of gravity and are detailed in the following section; M_p and M_r are the pitching and rolling body aerodynamic moments and are also detailed in the following section; u_a, v_a, and w_a are the body aerodynamic velocity components at the center of gravity of the projectile including the effect of atmospheric mean wind; X_w, Y_w, and Z_w are the total canard force components expressed in the body axis; and L_w, M_w, and N_w are the total canard moment components expressed in body coordinates. Note that the total canard forces and moments include contributions from all four canard lifting surfaces.

2.3 Body Aerodynamic Model.

A basic assumption in developing aerodynamic force and moment equations is that only two unique aerodynamic body force and moment components are generated, a drag and normal force, F_p and F_n, as well as a rolling and pitching moment, M_p and M_r. The body aerodynamic forces act at the center of gravity of the projectile. These forces can be visualized on the projectile in Figure 3. The projectile body aerodynamic force and moment expressions are given in Equations 25 through 28.

$$F_p = \frac{1}{2}\rho(u_a^2 + v_a^2 + w_a^2)\frac{\pi D^2}{4}C_{FP}(\alpha, M_a) \tag{25}$$

$$F_n = \frac{1}{2}\rho(u_a^2 + v_a^2 + w_a^2)\frac{\pi D^2}{4}C_{FN}(\alpha, M_a) \tag{26}$$

$$M_r = \frac{1}{2}\rho(u_a^2 + v_a^2 + w_a^2)\frac{\pi D^3}{4}C_{MR}(\alpha, M_a) \tag{27}$$

5

$$M_p = \frac{1}{2}\rho(u_a^2 + v_a^2 + w_a^2)\frac{\pi D^3}{4}C_{MP}(\alpha, M_a) \tag{28}$$

The reference diameter, D, used to nondimensionalize the projectile aerodynamic force and moment data is typically the cross-sectional diameter. As shown in Figure 3, the angle of attack of the projectile is defined as the angle between the relative wind velocity vector and the $\vec{\imath}_B$ axis. Using Figure 3 as a guide, the projectile angle of attack can be developed and is given by Equation 29.

$$\alpha = \tan^{-1}\frac{\sqrt{v_a^2 + w_a^2}}{u_a} \tag{29}$$

The local Mach number, M_a, at the projectile center of gravity is computed using Equation 30, which utilizes Equation 5 for the local speed of sound.

$$M_a = \frac{\|\vec{V}\|}{a} = \frac{\sqrt{u_a^2 + v_a^2 + w_a^2}}{49.0124\sqrt{T_0 + 0.003566z}} \tag{30}$$

The body aerodynamic velocity components expressed in the body reference frame including the effect of atmospheric mean wind are given by Equations 31 through 33.

$$u_a = u + V_{mw}\cos\theta\cos\psi\cos\psi_w + V_{mw}\cos\theta\sin\psi\sin\psi_w \tag{31}$$

$$v_a = v + V_{mw}(\sin\phi\sin\theta\cos\psi - \cos\phi\sin\psi)\cos\psi_w + V_{mw}(\sin\phi\sin\theta\sin\psi + \cos\phi\cos\psi)\sin\psi_w \tag{32}$$

$$w_a = w + V_{mw}(\cos\phi\sin\theta\cos\psi - \sin\phi\sin\psi)\cos\psi_w + V_{mw}(\cos\phi\sin\theta\sin\psi - \sin\phi\cos\psi)\sin\psi_w \tag{33}$$

As was previously defined, V_{mw} is the mean wind velocity at altitude and ψ_w is the azimuth angle at which the mean wind originates. See section 2.1 for a discussion of the atmosphere model. The projectile body aerodynamic force and moment coefficients are a function of both the local Mach number, M_a, and the angle of attack, α.

$$C_{FN} = c_{fn1}(M_a)\alpha + c_{fn3}(M_a)\alpha^3 + c_{fn5}(M_a)\alpha^5 \tag{34}$$

$$C_{FP} = c_{fp0}(M_a) + c_{fp2}(M_a)\alpha^2 \tag{35}$$

$$C_{MP} = c_{mp1}(M_a)\alpha + c_{mp3}(M_a)\alpha^3 + c_{mp5}(M_a)\alpha^5 + c_{mpq}(M_a)\frac{\sqrt{q^2 + r^2}D}{2\sqrt{u_a^2 + v_a^2 + w_a^2}} \tag{36}$$

$$C_{MR} = c_{mrd}(M_a) + c_{mrl}(M_a)\frac{pD}{2\sqrt{u_a^2 + v_a^2 + w_a^2}} \tag{37}$$

The aerodynamic coefficients, c_{fn1}, c_{fn3}, c_{fn5}, c_{fp0}, c_{fp2}, c_{mp1}, c_{mp3}, c_{mp5}, c_{mpq}, c_{mrd}, and c_{mrl}, are obtained through linear interpolation of a table of data that is a function of Mach number, M_a.

2.4 Canard Aerodynamic Model.

Both the total canard aerodynamic force vector, $\vec{F}_c = X_w\vec{\imath}_B + Y_w\vec{\jmath}_B + Z_w\vec{k}_B$, and the total canard aerodynamic moment vector, $\vec{M}_c = L_w\vec{\imath}_B + M_w\vec{\jmath}_B + N_w\vec{k}_B$, are summations of individual force and moment contributions from each canard lifting surface.

$$X_w = \sum_{i=1}^{N_c} X_{wi} \tag{38}$$

$$Y_w = \sum_{i=1}^{N_c} Y_{wi} \tag{39}$$

$$Z_w = \sum_{i=1}^{N_c} Z_{wi} \tag{40}$$
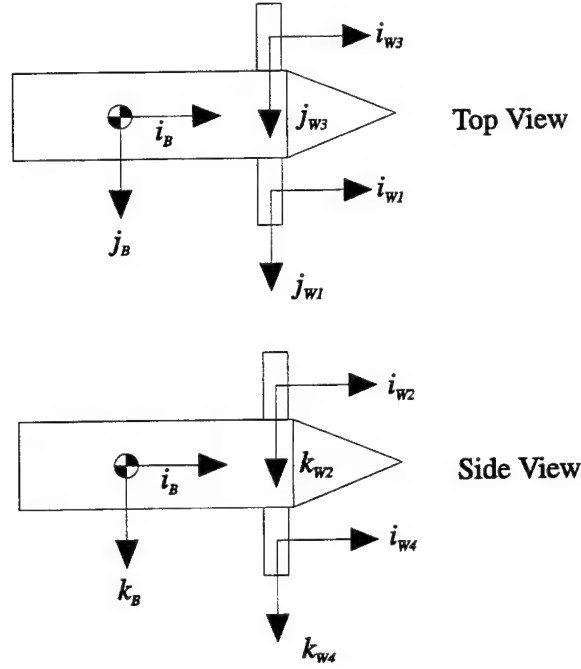
$$L_w = \sum_{i=1}^{N_c} L_{wi} \tag{41}$$

6

Figure 4: Canard geometry.

$$M_w = \sum_{i=1}^{N_c} M_{wi} \tag{42}$$

$$N_w = \sum_{i=1}^{N_c} N_{wi} \tag{43}$$

In Equations 38 through 43, N_c is the number of canard lifting surfaces. The current work uses four canards so that $N_c = 4$. The basic geometry of the canard lifting surfaces is shown in Figure 4. When the angular rates of the projectile are nonzero, each canard experiences a different aerodynamic velocity since each canard is located at a different position on the projectile body. Equations 44 through 47 provide generic formulas for the relative aerodynamic velocity components and the local Mach number of the ith canard needed for subsequent computation of canard aerodynamic forces and moments.

$$u_{ai} = u_a - rr_{yi} + qr_{zi} \tag{44}$$

$$v_{ai} = v_a + rr_{xi} - pr_{zi} \tag{45}$$

$$w_{ai} = w_a - qr_{xi} + pr_{yi} \tag{46}$$

$$M_i = \frac{\sqrt{u_{ai}^2 + v_{ai}^2 + w_{ai}^2}}{49.0124\sqrt{T_0 + 0.003566z}} \tag{47}$$

In Equations 44 through 46, r_{xi}, r_{yi}, and r_{zi} are components of the vector from the projectile center of gravity to the computation point on the ith canard lifting surface expressed in body coordinates.

Note that small differences in each canard's altitude create very small differences in atmospheric mean wind velocity magnitude, which, ultimately, also modifies the relative velocity experienced by a canard. However, this effect is believed to be very small and not taken into account. It is assumed that each canard experiences the identical atmospheric velocity field and density as the projectile center of gravity. In other words, at any time instant, the density and atmospheric velocity are assumed constant over the projectile and equal to that experienced by the projectile center of gravity.

7

As shown in Figure 4, the canards are not swept. Although in a general flight condition, the canard lifting surfaces encounter skewed flow, this effect is not modeled. Instead, it is assumed that canard aerodynamic lift and drag forces always lie in a plane parallel to the canards airfoil section. General formulas for the lift and drag forces generated by the ith canard are given in Equations 48 and 49.

$$L_i = \frac{1}{2}\rho(u_{ai}^2 + v_{ai}^2 + w_{ai}^2)S_i C_L \tag{48}$$

$$D_i = \frac{1}{2}\rho(u_{ai}^2 + v_{ai}^2 + w_{ai}^2)S_i C_D \tag{49}$$

In Equations 48 and 49, S_i represents wing surface area of the ith canard, and the aerodynamic lift and drag coefficients are given by Equations 50 and 51.

$$C_L = c_{la}(M_i)\alpha_i \tag{50}$$

$$C_D = c_{d0}(M_i) + c_{d2}(M_i)\alpha_i^2 + c_i(M_i)C_L^2 \tag{51}$$

The aerodynamic coefficients, c_{la}, c_{d0}, c_{d2}, and c_i, are obtained through linear interpolation of a table of data, which is a function of the local canard Mach number, M_i. It is important to note that due to the simple expansion of Equations 50 and 51 in α_i, the equations are only valid for small angles of attack. Because of slight differences in the formulas for computing aerodynamic forces and moments about the projectile's center of gravity, each canard lifting surface is developed separately in the following four subsections.

2.4.1 Canard 1.

As shown in Figure 5, the aerodynamic angle of attack of Canard 1 is given by Equation 52.

$$\alpha_1 = \delta_1 + \tan^{-1}\left(\frac{w_{a1}}{u_{a1}}\right) \tag{52}$$

The aerodynamic force and moment components are given by Equations 53 through 58.

$$X_{w1} = L_1 \frac{w_{a1}}{\sqrt{u_{a1}^2 + w_{a1}^2}} - D_1 \frac{u_{a1}}{\sqrt{u_{a1}^2 + w_{a1}^2}} \tag{53}$$

$$Y_{w1} = 0 \tag{54}$$

$$Z_{w1} = -L_1 \frac{u_{a1}}{\sqrt{u_{a1}^2 + w_{a1}^2}} - D_1 \frac{w_{a1}}{\sqrt{u_{a1}^2 + w_{a1}^2}} \tag{55}$$

$$L_{w1} = Z_{w1}r_{y1} - Y_{w1}r_{z1} \tag{56}$$

$$M_{w1} = X_{w1}r_{z1} - Z_{w1}r_{x1} \tag{57}$$

$$N_{w1} = Y_{w1}r_{x1} - X_{w1}r_{y1} \tag{58}$$

2.4.2 Canard 2.

As shown in Figure 6, the aerodynamic angle of attack of Canard 2 is given by Equation 59.

$$\alpha_2 = \delta_2 - \tan^{-1}\left(\frac{v_{a1}}{u_{a1}}\right) \tag{59}$$

The aerodynamic force and moment components are given by Equations 60 through 65.

$$X_{w2} = -L_2 \frac{v_{a2}}{\sqrt{u_{a2}^2 + v_{a2}^2}} - D_2 \frac{u_{a2}}{\sqrt{u_{a2}^2 + v_{a2}^2}} \tag{60}$$

$$Y_{w2} = L_2 \frac{u_{a2}}{\sqrt{u_{a2}^2 + v_{a2}^2}} - D_2 \frac{v_{a2}}{\sqrt{u_{a2}^2 + v_{a2}^2}} \tag{61}$$

$$Z_{w2} = 0 \tag{62}$$

$$L_{w2} = Z_{w2}r_{y2} - Y_{w2}r_{z2} \tag{63}$$

$$M_{w2} = X_{w2}r_{z2} - Z_{w2}r_{x2} \tag{64}$$

$$N_{w2} = Y_{w2}r_{x2} - X_{w2}r_{y2} \tag{65}$$

8

2.4.3 Canard 3.

As shown in Figure 7, the aerodynamic angle of attack of Canard 3 is given by Equation 66.

$$\alpha_3 = \delta_3 + \tan^{-1}\left(\frac{w_{a3}}{u_{a3}}\right) \tag{66}$$

The aerodynamic force and moment components are given by Equations 67 through 72.

$$X_{w3} = L_3 \frac{w_{a3}}{\sqrt{u_{a3}^2 + w_{a3}^2}} - D_3 \frac{u_{a3}}{\sqrt{u_{a3}^2 + w_{a3}^2}} \tag{67}$$

$$Y_{w3} = 0 \tag{68}$$

$$Z_{w3} = -L_3 \frac{u_{a3}}{\sqrt{u_{a3}^2 + w_{a3}^2}} - D_3 \frac{w_{a3}}{\sqrt{u_{a3}^2 + w_{a3}^2}} \tag{69}$$

$$L_{w3} = Z_{w3}r_{y3} - Y_{w3}r_{z3} \tag{70}$$

$$M_{w3} = X_{w3}r_{z3} - Z_{w3}r_{x3} \tag{71}$$

$$N_{w3} = Y_{w3}r_{x3} - X_{w3}r_{y3} \tag{72}$$

2.4.4 Canard 4.

As shown in Figure 8, the aerodynamic angle of attack of Canard 4 is given by Equation 73.

$$\alpha_4 = \delta_4 - \tan^{-1}\left(\frac{v_{a4}}{u_{a4}}\right) \tag{73}$$

The aerodynamic force and moment components are given by Equations 74 through 79.

$$X_{w4} = -L_4 \frac{v_{a4}}{\sqrt{u_{a4}^2 + v_{a4}^2}} - D_4 \frac{u_{a4}}{\sqrt{u_{a4}^2 + v_{a4}^2}} \tag{74}$$

$$Y_{w4} = L_4 \frac{u_{a4}}{\sqrt{u_{a4}^2 + v_{a4}^2}} - D_4 \frac{v_{a4}}{\sqrt{u_{a4}^2 + v_{a4}^2}} \tag{75}$$

$$Z_{w4} = 0 \tag{76}$$

$$L_{w4} = Z_{w4}r_{y4} - Y_{w4}r_{z4} \tag{77}$$

$$M_{w4} = X_{w4}r_{z4} - Z_{w4}r_{x4} \tag{78}$$

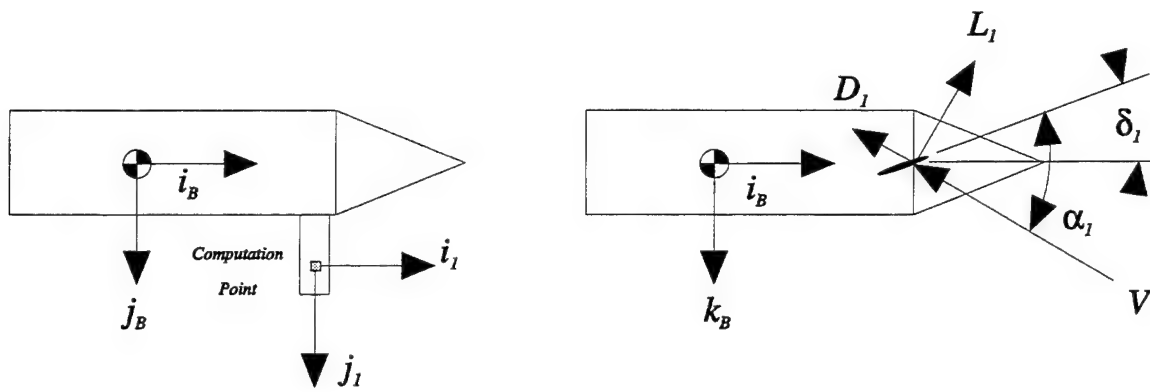$$N_{w4} = Y_{w4}r_{x4} - X_{w4}r_{y4} \tag{79}$$
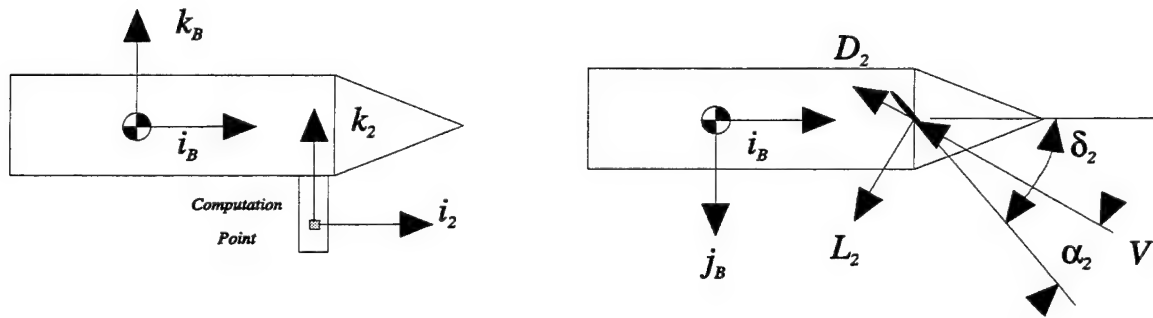
Figure 5: Canard 1 geometry.
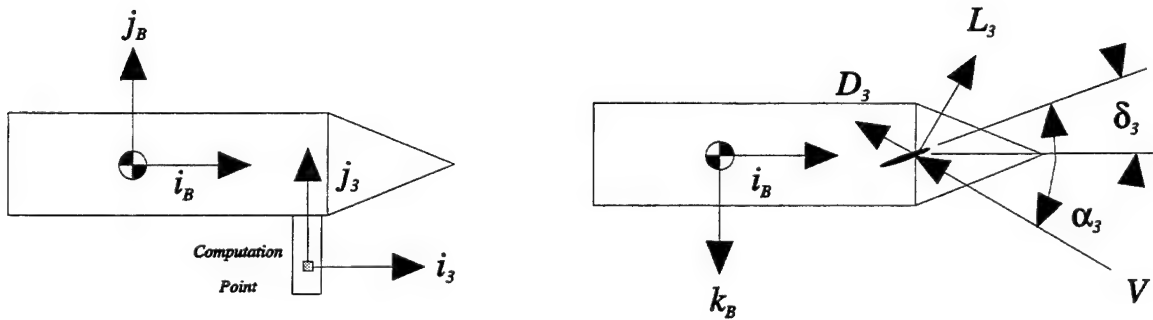

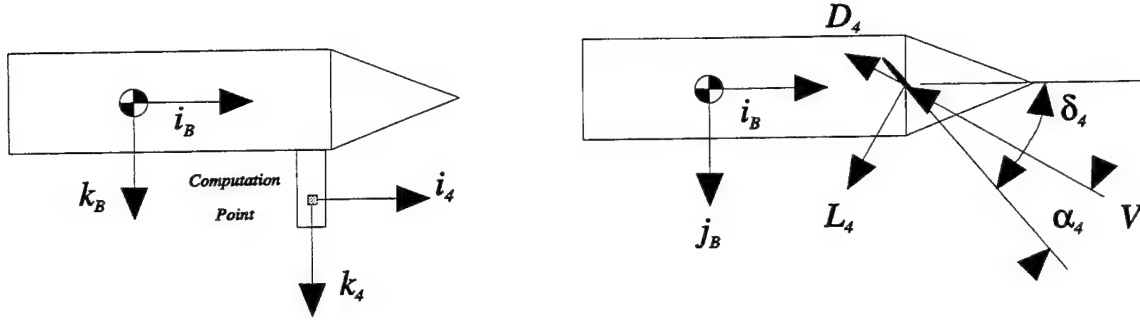Figure 6: Canard 2 geometry.

Figure 7: Canard 3 geometry.

Figure 8: Canard 4 geometry.

2.5 Control System Model

There are three options when computing projectile trajectory simulations using the movable canards. The first option is to eliminate the canards from the simulation. In this case, the simulation becomes a standard six-degree-of-freedom projectile simulation. The second option is to allow the canards to be set at predetermined deflection angles as a function of time. Because the canard angular deflections would not depend on the state of the projectile, this type of control does not involve sensor feedback and is denoted the open loop control case. The third option is to compute the canard deflection angles using an automatic flight control system that utilizes sensor feedback to drive the trajectory of the projectile toward a prespecified desired trajectory. This third case is denoted the closed loop control case.

The purpose of the closed loop projectile control system is to first generate a desired trajectory and second to command the controllable canard lifting surfaces in such a way as to follow the desired path. The trajectory command methodology and projectile feedback control laws are presented in the following two subsections, respectively.

2.5.1 Command Trajectory Model

A desired trajectory can be prescribed by a set of inertial guidance points that the projectile should fly through. Figure 9 shows an example desired trajectory as specified by six points in space. For the present study, only two-dimensional command trajectories were used. However, the methodology can be extended to three-dimensional trajectories in a straightforward manner. The commanded inertial position at some instant in time is computed such that it leads the projectile by some buffer distance, B_u, along the desired path. It is analogous to a "donkey chasing hay" scenario. Figure 10 illustrates the geometry involved in solving for the command coordinates. Noting Figure 10, along a particular line segment, the trajectory line is given by Equation 80.

$$\Delta x \; z_T - \Delta z \; x_T - b_T = 0 \tag{80}$$

In Equation 80, Δx and Δz are changes in the trajectory line segment coordinates from the end edge point to the start edge point. Obviously, Δx and Δz can be different for each trajectory line segment. A projection line can be formed, which passes through the current position of the projectile and at the same time is perpendicular to the current tracking line. The projection line is given by Equations 81 and 82.

$$\Delta z \; z_T + \Delta x \; x_T - a_T = 0 \tag{81}$$

$$a_T = \Delta z \; z + \Delta x \; x \tag{82}$$

Recall that x, y, and z are components of the inertial position vector of the projectile center of gravity. The projection point (x_p, z_p) is defined as the point of intersection between the tracking and projection line. It is arrived at by equating the tracking line and the projection line. Equations 83 and 84 provide formulas for computing x_p and z_p, respectively.

$$x_p = \frac{a_T \; \Delta x - b_T \; \Delta z}{\Delta x^2 + \Delta z^2} \tag{83}$$
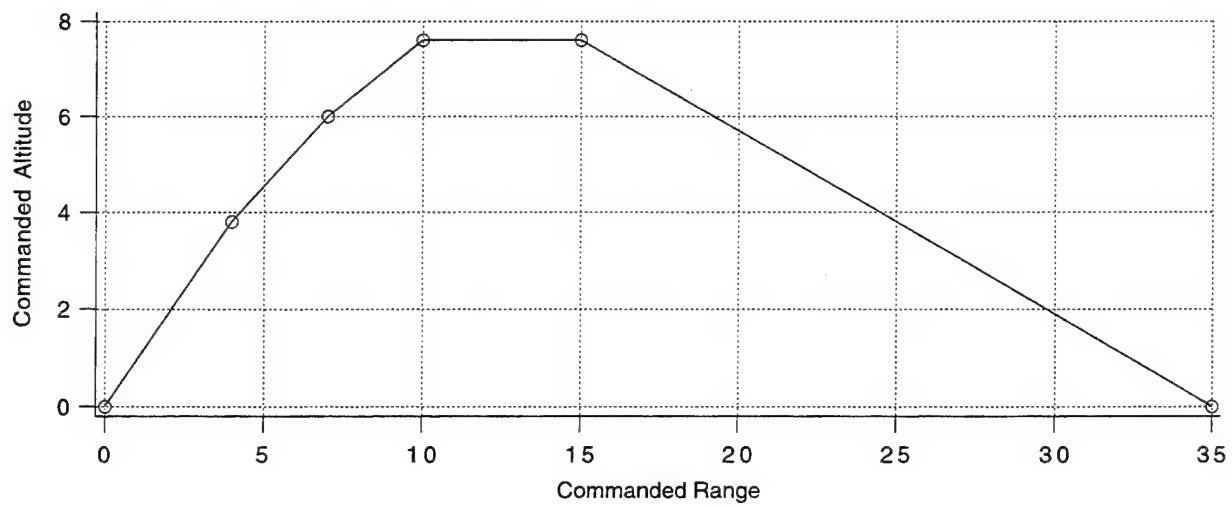
11

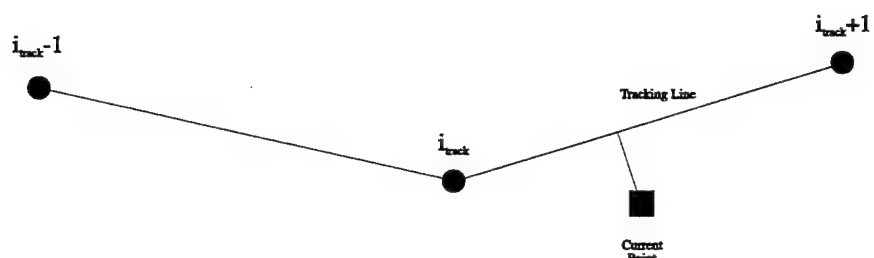Figure 9: Example command trajectory.

Figure 10: Command trajectory line segment geometry.

12

$$z_p = \frac{a_T \ \Delta z + b_T \ \Delta x}{\Delta x^2 + \Delta z^2} \tag{84}$$

The commanded inertial position leads the projection point by the distance B_u along the tracking line. There are two cases that must be considered. The first case is where the distance from the projection point to the tracking line segment edge point is greater than the buffer distance. In this case the inertial position command, x_c and z_c, will be on the same line as the projection point and Equations 85 and 86 provide the formulas for computation.

$$x_c = x_p + \frac{B_u}{\sqrt{1 + \left(\frac{\Delta z}{\Delta x}\right)^2}} \tag{85}$$

$$z_c = z_p + \frac{B_u}{\sqrt{1 + \left(\frac{\Delta x}{\Delta z}\right)^2}} \tag{86}$$

The second case that must be considered is where the distance from the projection point to the tracking line segment end edge point, which we shall denote as d_T, is less than the buffer distance, B_u. In this case, the current tracking line segment is incremented and the command point is now along the new tracking line segment. Denote the new tracking line segment start point as (x_s, z_s). The command point is computed starting from (x_s, z_s) and using an equivalent buffer distance equal to $B_u - d_t$. Equations 87 and 88 provide formulas for computation.

$$x_c = x_s + \frac{B_u - d_T}{\sqrt{1 + \left(\frac{\Delta z}{\Delta x}\right)^2}} \tag{87}$$

$$z_c = z_s + \frac{B_u - d_T}{\sqrt{1 + \left(\frac{\Delta x}{\Delta z}\right)^2}} \tag{88}$$

Note that in either case the cross range command, y_c, will be identically zero, since only two-dimensional command trajectories are being considered.

2.5.2   Feedback Control Law Model

In section 2.4, expressions for canard aerodynamic forces and moments exerted on the projectile body were developed. These forces and moments are a function of canard rotation angles, δ_1, δ_2, δ_3, and δ_4, corresponding to the four canards. Judicious rotation of the canards can modify the path of the projectile in a desirable fashion. The purpose of the feedback control laws is to command canard rotation angles so that the projectile does, in fact, follow the commanded inertial path to within a specified accuracy. The feedback control law mathematical model used in the current effort utilizes inertial position and velocity feedback, roll rate feedback, and Euler angle feedback. Thus, x, y, z, $\dot{x}$, $\dot{y}$, $\dot{z}$, p, ϕ, θ, and ψ are assumed available for use in the control law model. The basic control law philosophy is to eliminate the angle between the projectile velocity vector and the position vector from the projectile center of gravity to the trajectory command point. To this end, the inertial position error vector, $\{e_x \ e_y \ e_z\}$, is expressed in projectile body coordinates using Equations 89 through 91.

$$e_x = \cos\theta\cos\psi(x_c - x) + \cos\theta\sin\psi(y_c - y) - \sin\theta(z_c - z) \tag{89}$$

$$e_y = (\sin\phi\sin\theta\cos\psi - \cos\phi\sin\psi)(x_c - x) + (\sin\phi\sin\theta\sin\psi + \cos\phi\cos\psi)(y_c - y) + \sin\phi\cos\theta(z_c - z) \tag{90}$$

$$e_z = (\cos\phi\sin\theta\cos\psi + \sin\phi\sin\psi)(x_c - x) + (\cos\phi\sin\theta\sin\psi - \sin\phi\cos\psi)(y_c - y) + \cos\phi\cos\theta(z_c - z) \tag{91}$$

Equations 92 through 94 provide expressions for the control system estimate of the projectile velocity vector expressed in body coordinates.

$$u_{cs} = \cos\theta\cos\psi\dot{x} + \cos\theta\sin\psi\dot{y} - \sin\theta\dot{z} \tag{92}$$

$$v_{cs} = (\sin\phi\sin\theta\cos\psi - \cos\phi\sin\psi)\dot{x} + (\sin\phi\sin\theta\sin\psi + \cos\phi\cos\psi)\dot{y} + \sin\phi\cos\theta\dot{z} \tag{93}$$

$$w_{cs} = (\cos\phi\sin\theta\cos\psi + \sin\phi\sin\psi)\dot{x} + (\cos\phi\sin\theta\sin\psi - \sin\phi\cos\psi)\dot{y} + \cos\phi\cos\theta\dot{z} \tag{94}$$

13

Note that u_{cs}, v_{cs}, and w_{cs} are computed by the control system but are in fact equal to u, v, and w, respectively. Using Equations 89 through 94, the pitch and yaw error angles are formed.

$$\theta_{ERR} = \tan^{-1}\left(\frac{w_{fil}}{u_{fil}}\right) - \tan^{-1}\left(\frac{e_z}{e_x}\right) \tag{95}$$

$$\psi_{ERR} = \tan^{-1}\left(\frac{e_y}{e_x}\right) - \tan^{-1}\left(\frac{v_{fil}}{u_{fil}}\right) \tag{96}$$

The quantities u_{fil}, v_{fil}, and w_{fil} are low pass filtered versions of u_{cs}, v_{cs}, and w_{cs} governed by Equations 97 through 99.

$$\tau_u \dot{u}_{fil} + u_{fil} = u_{cs} \tag{97}$$

$$\tau_v \dot{v}_{fil} + v_{fil} = v_{cs} \tag{98}$$

$$\tau_w \dot{w}_{fil} + w_{fil} = w_{cs} \tag{99}$$

In the previous equations, τ_u, τ_v, and τ_w are time constants chosen to optimize overall system performance. The control laws also utilize integrated roll rate (p_i), integrated pitch angle error (θ_{ERRI}), and integrated yaw angle error (ψ_{ERRI}) as given by Equations 100 through 102.

$$\dot{p}_i = p \tag{100}$$

$$\dot{\theta}_{ERRI} = \theta_{ERR} \tag{101}$$

$$\dot{\psi}_{ERRI} = \psi_{ERR} \tag{102}$$

The basic control laws are angular rate commands, e_p, e_q, and e_r, given by Equations 103 through 105.

$$e_p = K_p p + K_{pi} p_i + K_\phi \phi \tag{103}$$

$$e_q = K_\theta \theta_{ERR} + K_{\theta_i} \theta_{ERRI} \tag{104}$$

$$e_r = K_\psi \psi_{ERR} + K_{\psi_i} \psi_{ERRI} \tag{105}$$

In the previous equations, K_p, K_{pi}, K_ϕ, K_θ, K_{θ_i}, K_ψ, and K_{ψ_i} are feedback control law gains and are set to optimize system performance. To form the final canard rotation angles, Equations 106 through 109 are used.

$$\delta_1 = e_q - e_p \tag{106}$$

$$\delta_2 = e_r + e_p \tag{107}$$

$$\delta_3 = e_q + e_p \tag{108}$$

$$\delta_4 = e_r - e_p \tag{109}$$

The canard rotation angles are limited to lie between a predetermined constant, $\pm\delta_{LIMIT}$.

2.6 Solution Technique.

The mathematical equations developed previously represent an initial value problem comprised of 18 coupled ordinary differential equations. Due to the difficulty in obtaining a closed form analytic solution to these equations, a numerical approach is taken to compute both time simulation and linear dynamic models of the system. A computer program was developed to perform the computations. The code, dubbed BOOM, is written in portable FORTRAN and has no calls to routines not contained in the source code file.

2.6.1 Time Simulation.

To simplify the discussion to follow, vector notation will be utilized. Define ζ as a vector containing the state variables of the problem.

$$\zeta = [x \ y \ z \ \phi \ \theta \ \psi \ u \ v \ w \ p \ q \ r \ p_i \ \theta_{ERRI} \ \psi_{ERRI} \ u_{fil} \ v_{fil} \ w_{fil}]^T \tag{110}$$

Let ϑ be a vector containing the canard control deflections.

$$\vartheta = [\delta_1 \ \delta_2 \ \delta_3 \ \delta_4] \tag{111}$$

The initial value problem previously developed can be cast in the form shown in Equations 112 and 113.

$$\dot{\zeta} = f(\zeta, \vartheta) \tag{112}$$

$$\zeta(t = 0) = \zeta_0 \tag{113}$$

For time simulation, Equation 112 is integrated numerically in time using Newton's method with initial conditions specified through Equation 113. The recursion formula is given in Equation 114.

$$\zeta(t + \Delta t) = \zeta(t) + \Delta t f(\zeta(t), \vartheta(t)) \tag{114}$$

The time simulation software was verified by a hand calculation through one time step using a random, nonzero state and nonzero input parameters.

2.6.2 Linear Models.

At any time step in the simulation described previously, denote the current state as $\bar{\zeta}$. A linear dynamic model can be formed that is valid in a small neighborhood around $\bar{\zeta}$.

$$\frac{\partial \tilde{\zeta}}{\partial t} = \left[\frac{\partial f}{\partial \zeta}\right] \tilde{\zeta}(t) + \left[\frac{\partial f}{\partial \vartheta}\right] \tilde{\vartheta}(t) \tag{115}$$

The state variables and control deflections can then be constructed using Equations 116 and 117.

$$\zeta(t) = \bar{\zeta} + \tilde{\zeta}(t) \tag{116}$$

$$\vartheta(t) = \bar{\vartheta} + \tilde{\vartheta}(t) \tag{117}$$

The matrices $\frac{\partial f}{\partial \zeta}$ and $\frac{\partial f}{\partial \vartheta}$ are the system dynamics and control matrices, respectively. Eigenvalues of the system dynamics matrix yield the modes of the system, which include stability information, while the control matrix is useful in determining initial control system gain values. Notice that the linearization is not performed about a steady state condition as is usually the case in aircraft linear models but rather an instant in time where the system state is changing. Thus, information derived from the linear model, such as frequency and damping of projectile modes, is valid for the instant in time at linearization. The system dynamics and control matrices are computed using a forward difference. Equations 118 and 119 provide the formulas for computing the (i, j) components of the dynamics and control matrices, respectively.

$$\frac{\partial f_i}{\partial \zeta_j} = \frac{f_i(\bar{\zeta} + \epsilon_j, \bar{\vartheta}) - f_i(\bar{\zeta}, \bar{\vartheta})}{\epsilon_j} \tag{118}$$

$$\frac{\partial f_i}{\partial \vartheta_j} = \frac{f_i(\bar{\zeta}, \bar{\vartheta} + \varepsilon_j) - f_i(\bar{\zeta}, \bar{\vartheta})}{\varepsilon_j} \tag{119}$$

In Equations 118 and 119, ϵ_j and ε_j are perturbation vectors such that all components are zero except the jth component, which is a small perturbation value.

3 Results.

Time simulation results were generated for an extended range projectile, which is currently under development. Basic technical data on the projectile is given in Table 1. The body aerodynamic coefficient data is given in Figures 11 through 21. The body aerodynamic was generated using the computer code PRODAS. Note that the PRODAS generated body aerodynamic data is an estimation based on theoretical and empirical data sources. It is not the results of the projectile in a firing range or in a wind tunnel.

Table 1: Extended Range Projectile Parameter Values

| Parameter	Symbol	Units	Value
Projectile Reference Diameter	D	ft	0.5
Mass of Projectile	m	slug	3.98
Roll Moment of Inertia	I_{xx}	slug ft^2	4.13
Pitch Moment of Inertia	I_{yy}	slug ft^2	352.0
Yaw Moment of Inertia	I_{zz}	slug ft^2	352.0
Canard 1 Wing Area	S_1	ft^2	0.1052
Canard 2 Wing Area	S_2	ft^2	0.1052
Canard 3 Wing Area	S_3	ft^2	0.1052
Canard 4 Wing Area	S_4	ft^2	0.1052
Component of Distance from C.G. to Canard 1	r_{x1}	ft	2.37
Component of Distance from C.G. to Canard 1	r_{y1}	ft	0.51
Component of Distance from C.G. to Canard 1	r_{z1}	ft	0.00
Component of Distance from C.G. to Canard 2	r_{x2}	ft	2.37
Component of Distance from C.G. to Canard 2	r_{y2}	ft	0.00
Component of Distance from C.G. to Canard 2	r_{z2}	ft	-0.51
Component of Distance from C.G. to Canard 3	r_{x3}	ft	2.37
Component of Distance from C.G. to Canard 3	r_{y3}	ft	-0.51
Component of Distance from C.G. to Canard 3	r_{z3}	ft	0.00
Component of Distance from C.G. to Canard 4	r_{x4}	ft	2.37
Component of Distance from C.G. to Canard 4	r_{y4}	ft	0.00
Component of Distance from C.G. to Canard 4	r_{z4}	ft	0.51
Roll Rate Gain	k_p	nd	-1.00
Integrated Roll Rate Gain	k_{pi}	nd	0.00
Roll Angle Gain	k_ϕ	nd	-0.70
Pitch Angle Error Gain	k_θ	nd	0.04
Integrated Pitch Angle Error Gain	k_{θ_i}	nd	0.002
Yaw Angle Error Gain	k_ψ	nd	0.04
Integrated Yaw Angle Error Gain	k_{ψ_i}	nd	0.002
Canard Deflection Limit	δ_{LIMIT}	rad	0.17
Forward Velocity Time Constant	τ_u	nd	0.1
Side Velocity Time Constant	τ_v	nd	0.1
Vertical Velocity Time Constant	τ_w	nd	0.1
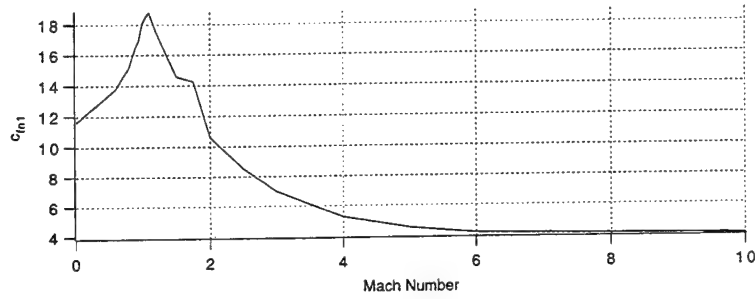
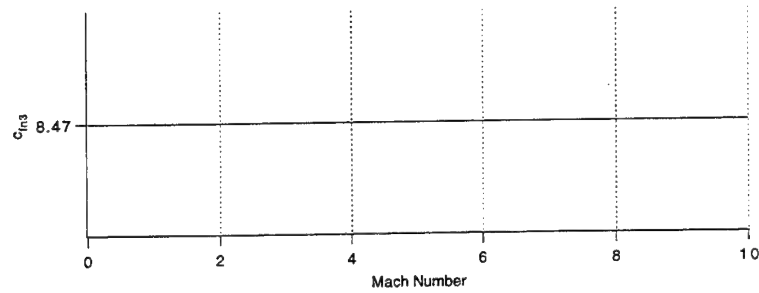Figure 11: Projectile body aerodynamic coefficient c_{fn1} vs. Mach number.

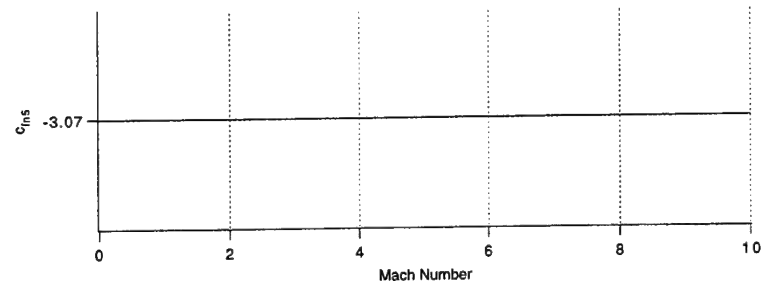Figure 12: Projectile body aerodynamic coefficient c_{fn3} vs. Mach number.

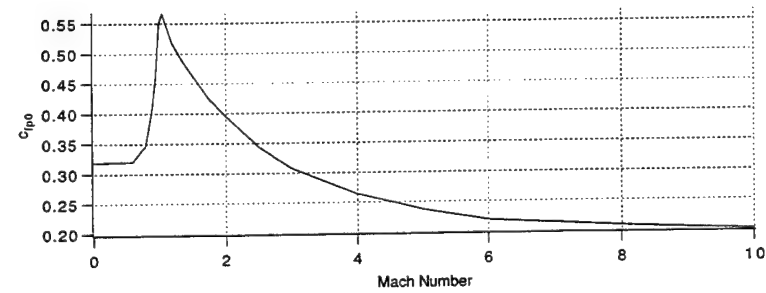Figure 13: Projectile body aerodynamic coefficient c_{fn5} vs. Mach number.

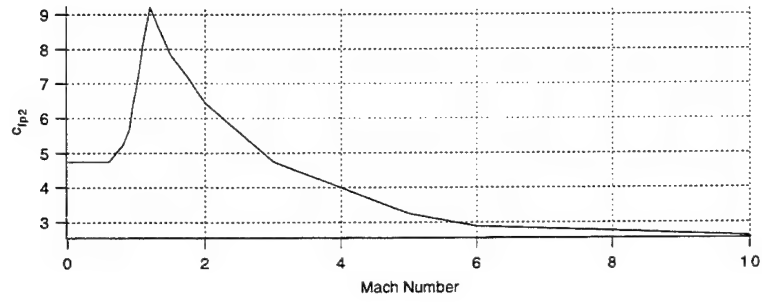Figure 14: Projectile body aerodynamic coefficient c_{fp0} vs. Mach number.

17

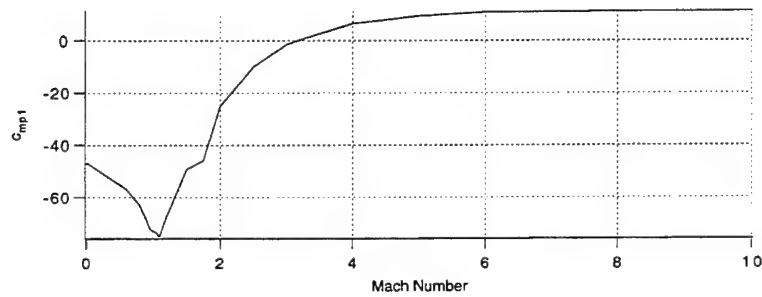Figure 15: Projectile body aerodynamic coefficient c_{fp2} vs. Mach number.

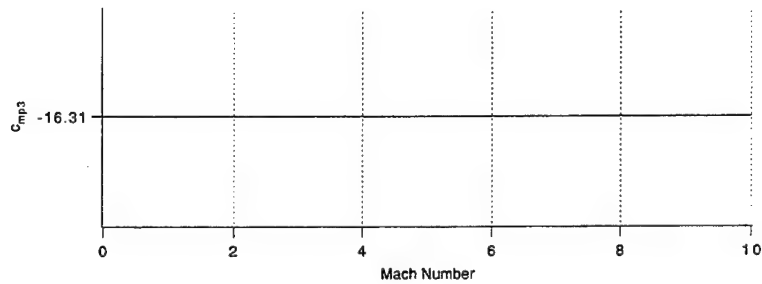Figure 16: Projectile body aerodynamic coefficient c_{mp1} vs. Mach number.

Figure 17: Projectile body aerodynamic coefficient c_{mp3} vs. Mach number.
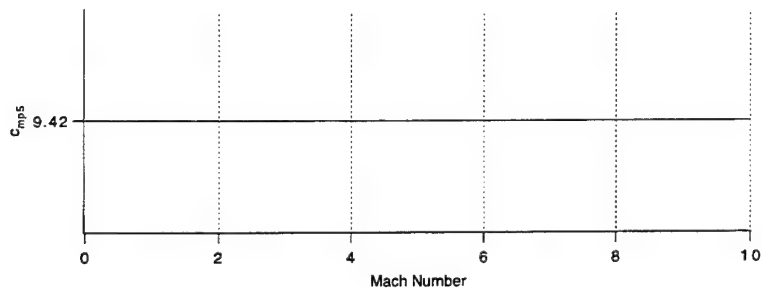

Figure 18: Projectile body aerodynamic coefficient c_{mp5} vs. Mach number.
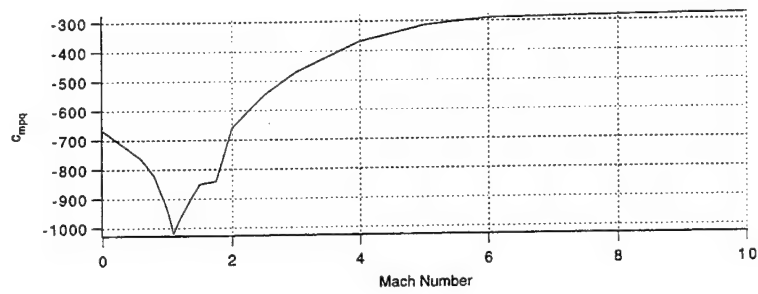
18

Figure 19: Projectile body aerodynamic coefficient c_{mpq} vs. Mach number.
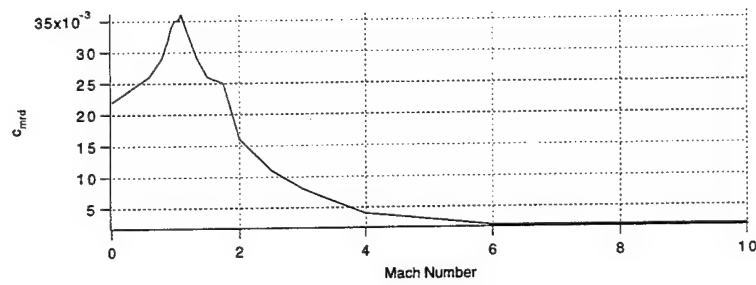

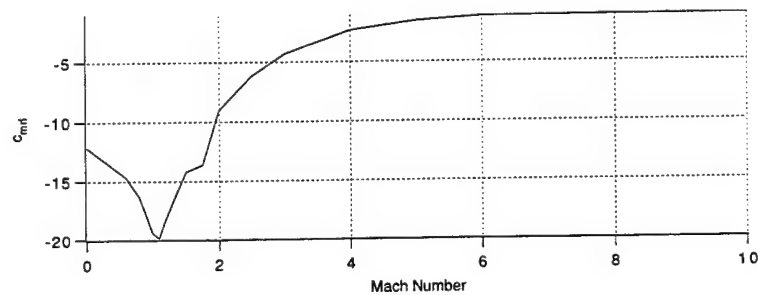Figure 20: Projectile body aerodynamic coefficient c_{mrd} vs. Mach number.

Figure 21: Projectile body aerodynamic coefficient c_{mrl} vs. Mach number

Time simulation results were generated for the extended range projectile in both partially closed and fully closed loop configurations. The 128-lb projectile is 79 in long, has a diameter of 6 in, and is similar in shape to a standard projectile fired from a 155-mm gun. Four canards, each with a surface area of 15 in^2, were used to control the projectile. For this projectile, a canard surface area of 15 in^2 represents a practical upper limit on what could be installed in a production round. Time histories of all the state variables are plotted for the partially closed loop configuration in Figures 22 through 27. At the apex of flight, the partially closed loop configuration injects a pitch command of 5.7° to effect a pitch up maneuver. Note that prior to the apex of flight a closed loop roll channel control system using roll rate, roll angle, and integrated roll rate eliminates both roll rate and roll angle of the projectile. Initial conditions for the simulation results shown in Figures 22 through 27 are as follows: $x = y = z = \phi = \psi = v = w = q = r = 0$, $u = 2788$ fps, $\theta = 45°$, $p = 31$ r/s. Figure 22 shows the range, altitude, and cross range of the projectile in the partially closed loop configuration. The range time history in Figure 22 compares the range of the projectile with and without the movable canards installed. Under the conditions mentioned previously, the estimated range extension is 148%. The small discrepancy between the baseline and controlled time histories before the onset of the pitch command is due to the drag of the canards, which are not present on the baseline projectile. From the altitude plot, it can be seen that the time of flight of the projectile dramatically increases from 79 s to 351 s. The cross range of the projectile is slightly over 1.6 km at the terminal point. Subsequent to the execution of the pitch command, a slight steady state yaw rate develops that alters the azimuth of the projectile hence creating a dispersion in the cross range.

Figure 23 shows the body attitudes for the partially closed loop simulation set. From the roll angle trace, it is seen that the roll channel control system eliminates the projectile roll rate and roll angle within 10 s. Also in Figure 23, the pitch attitude of the baseline trajectory is compared with the controlled trajectory. At launch, both trajectories have a 45° pitch attitude; however, the baseline trajectory pitch attitude monotonically decreases with time, whereas the controlled trajectory experiences some transient oscillations immediately after the pitch command is executed. After the transient oscillations die out, the controlled trajectory pitch attitude settles to a value of -2.3° in the steady state glide portion of flight. Figure 23 also plots the yaw attitude as a function of time. From the yaw attitude plot, it is seen that yaw attitude remains very small until the pitch command is executed at which time a small steady state yaw rate develops, which induces a continuously increasing yaw attitude response with time.

Figure 24 shows the three components of the body velocity vector for the partially closed-loop case. The forward velocity trace is interesting as it compares the baseline and controlled simulation results. The baseline trajectory arrives at the terminal point ($z = 0$) at $t = 79$ s which corresponds to a terminal velocity of 309.6 m/s, while the terminal point ($z = 0$) of the controlled trajectory occurs at $t = 351$ s, which corresponds to a terminal velocity of 105.7 m/s. Thus, the controlled trajectory has a significant decrease in forward velocity at the impact point. Furthermore, the decreased velocity is present throughout a large portion of the flight. The body side velocity shown in Figure 24 remains very small throughout the entire trajectory with some small transient vibration occurring at launch and at the onset of the pitch command at $t = 38$ s. The body vertical velocity is also shown on Figure 24. While not shown on Figure 24, the baseline vertical velocity is very small, since the angle of attack of the baseline trajectory is also very small. In contrast, the vertical velocity of the controlled trajectory attains a maximum velocity of 75 m/s at the onset of the pitch maneuver. The controlled trajectory vertical velocity is due to the pitch command maneuver, which causes an angle of attack to be developed on the projectile, which, in turn, dictates that the relative velocity have nonzero components along the axis of symmetry of the projectile and along the $\bar{k}_B$ axis. As the projectile angle of attack increases, a commensurate increase in the vertical velocity is to be expected.

Figure 25 plots the components of the angular velocity vector for the partially closed loop projectile configuration. It is seen from the roll rate time history that the action of the canards is to very rapidly eliminate the roll rate from 31 rad/s to 0 within 10 s. This is absolutely necessary for the partially closed-loop configuration, since the pitch attitude commands assume the projectile will maintain zero roll rate and angle from the start of pitch commands to the terminal point. Pitch rate of the projectile is also plotted in Figure 25 and shows that pitch rate jumps to 17.3°/s at the onset of the pitch command and eventually damps to zero approximately 200 s after launch. Figure 25 also plots yaw rate of the controlled projectile. At launch, yaw rate jumps to 0.7°/s due to yaw/roll coupling, but as roll rate decreases, the yaw rate settles to a small value of 0.02°/s. At $t = 38$ s, a transient in yaw rate is caused by the abrupt pitch command. It

is the small yaw rate which persists throughout most of the flight, that causes monotonically increasing yaw attitude and significant cross range dispersion at the terminal point.

Figure 26 shows the aerodynamic angle of attack of the projectile body as a function of time for the partially closed loop configuration. While the baseline trajectory angle of attack is not overlaid on this plot, it is very small (less than 1° over the entire time history). The angle of attack of the projectile body is shown to be very small initially until the pitch command is executed, at which time, the angle of attack increases to a maximum of 18.8°. Note that the canard model used in the current effort is only valid for small angles of attack below 15°. As the canard angle of attack will basically follow the projectile body angle of attack, the canards will be stalled during the high angle of attack portions of the transient response. This effect is not modeled and may influence the results. Figure 26 plots the canard deflection for the partially closed loop case. To zero roll rate and roll angle, canards 2 and 3 deflect identically, while canards 1 and 4 also deflect identically but in the opposite direction as canards 2 and 3. Since canards 1 and 3 are in the pitch plane of the projectile and effect pitch maneuvers, they are deflected by 5.7° ± the canard deflection to null roll rate. A nonzero canard deflection is necessary to null roll rate in the steady state, because the aft fins on the projectile have an effective cant of 0.29°.

Figures 22 through 26, show that the range of a projectile can be significantly increased by using body lift achieved by pitching the projectile upward using the movable canard lifting surfaces. While a dramatic increase in range is achievable, an equally dramatic increase in the time of flight and decrease in the impact point velocity is realized. Thus, the action of the movable canards is to facilitate a transfer of kinetic energy to potential energy, allowing the projectile to stay aloft longer. If a higher impact velocity or a shorter time of flight is desired, then a subsequent decrease in the maximum range will follow.
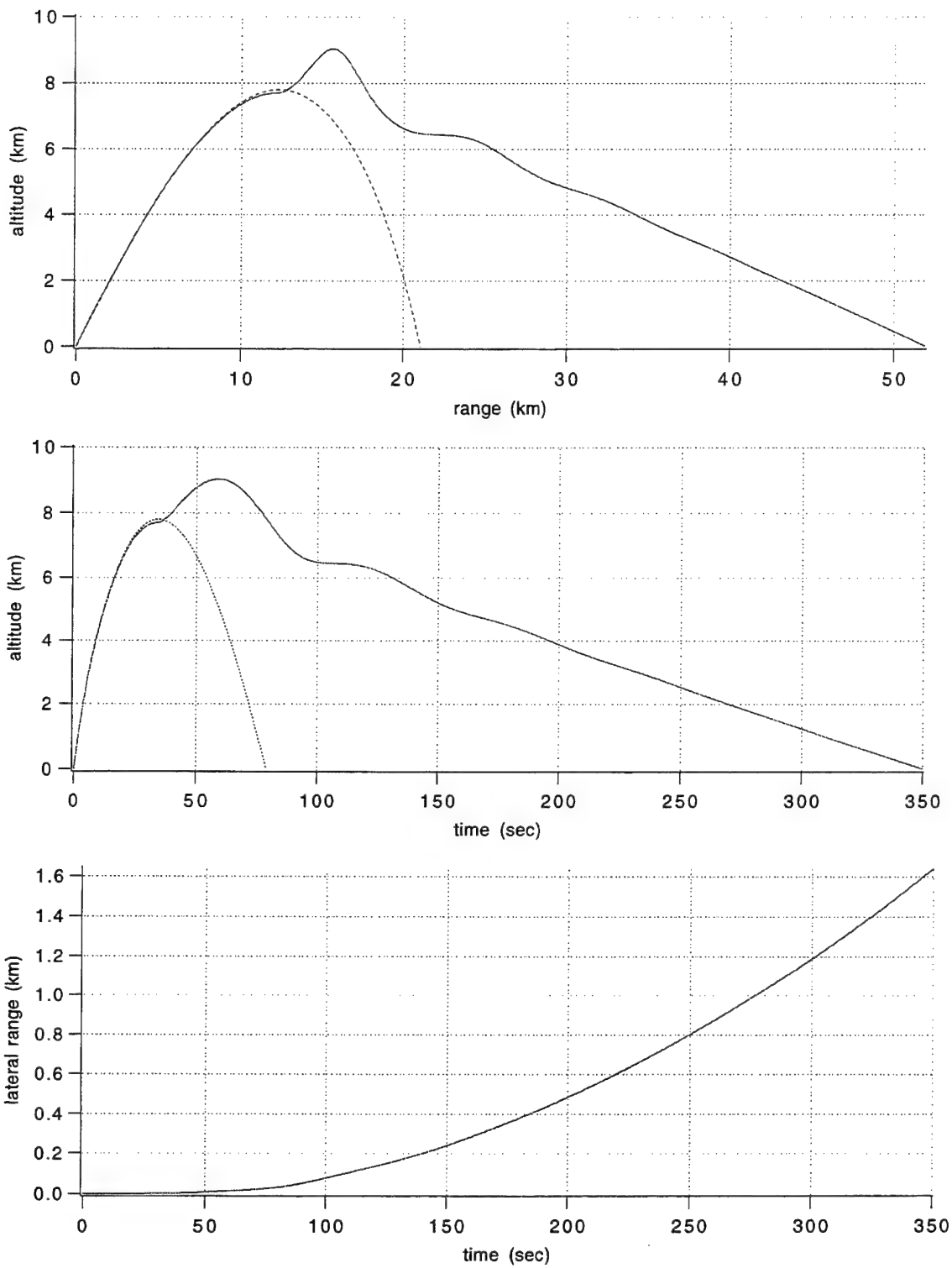
Figure 22: Partially closed-loop range extension, position (solid = controlled, dotted = baseline).
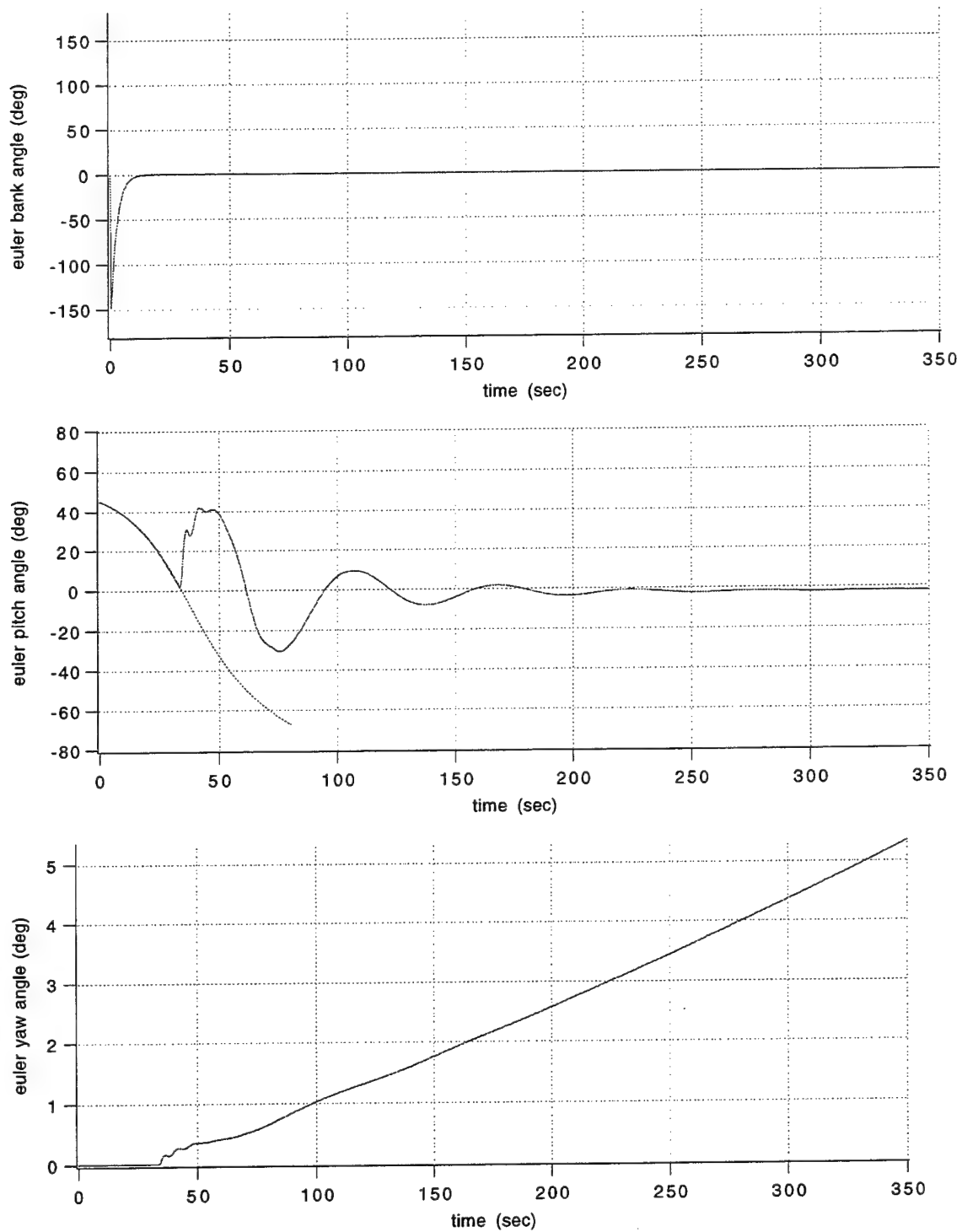
Figure 23: Partially closed-loop range extension, Euler angles (solid = controlled, dotted = baseline).
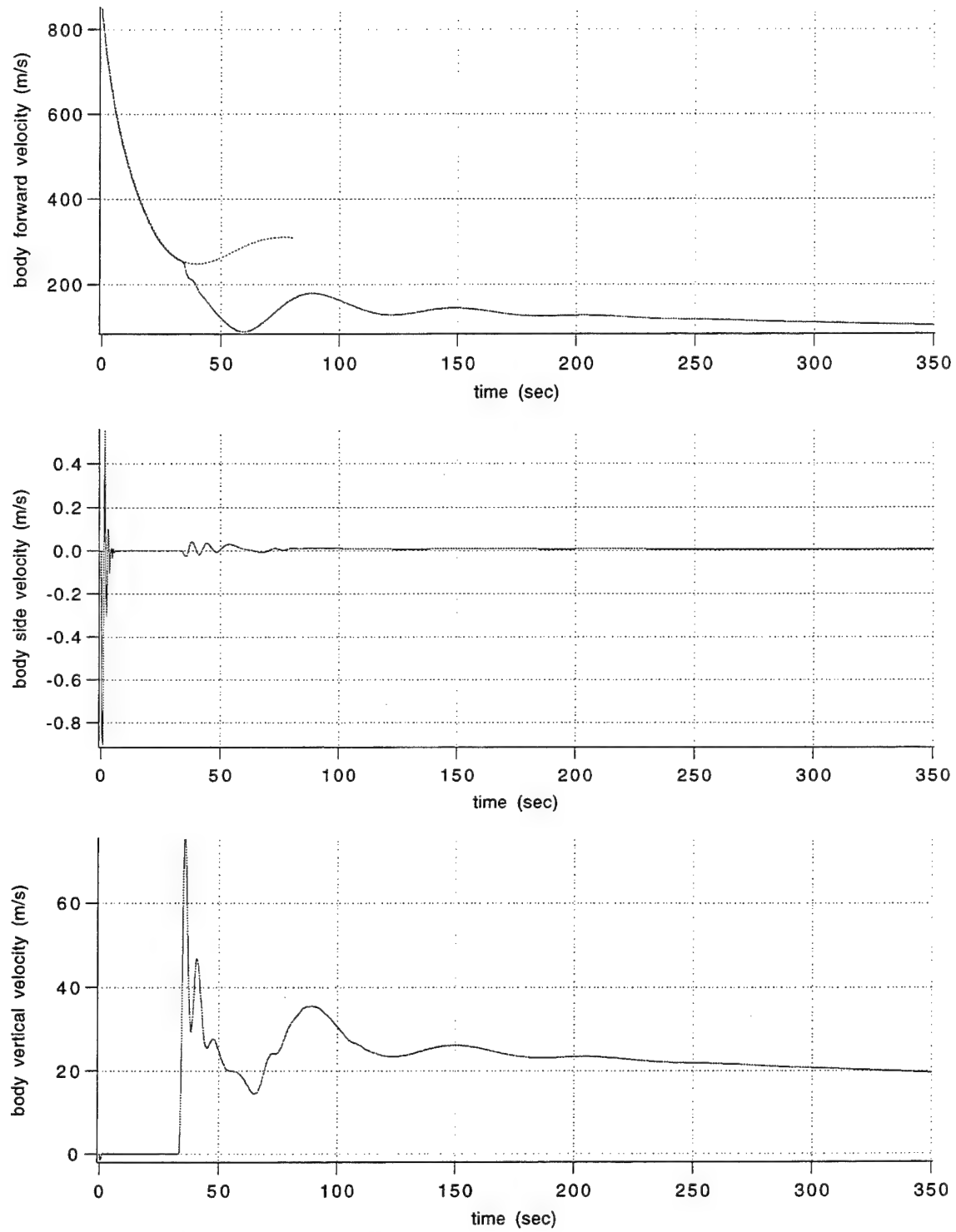
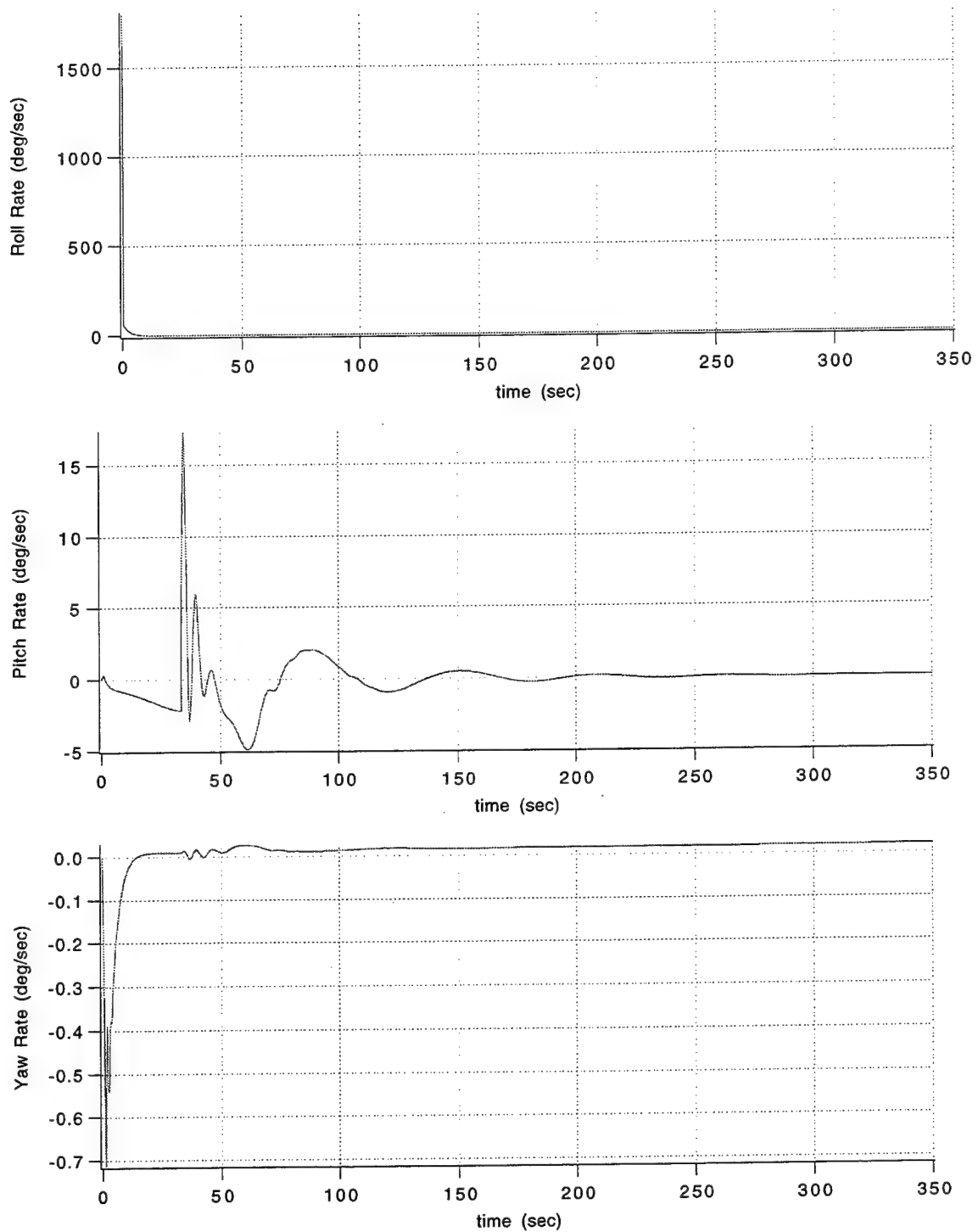Figure 24: Partially closed-loop range extension, body velocity (solid = controlled, dotted = baseline).

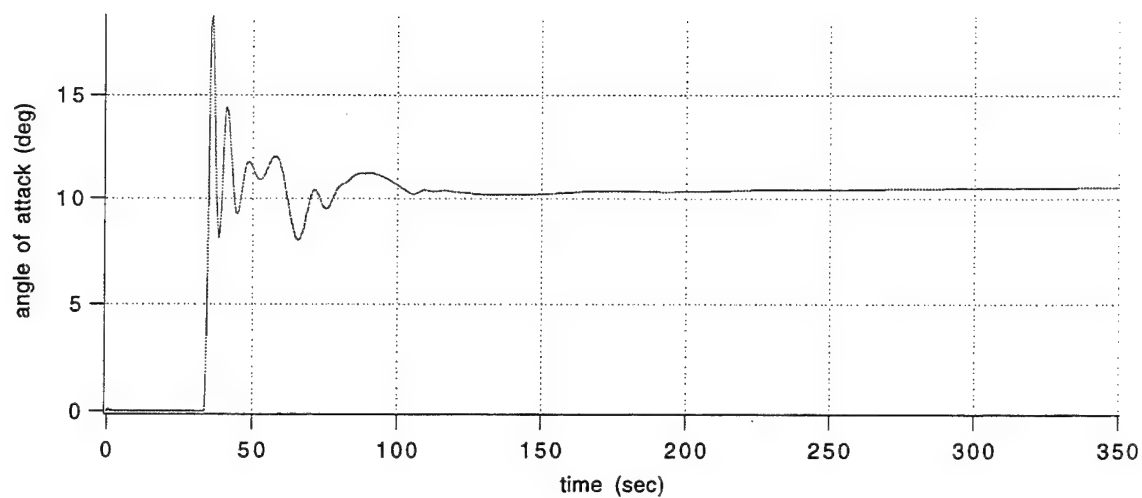Figure 25: Partially closed-loop range extension, body angular velocity.

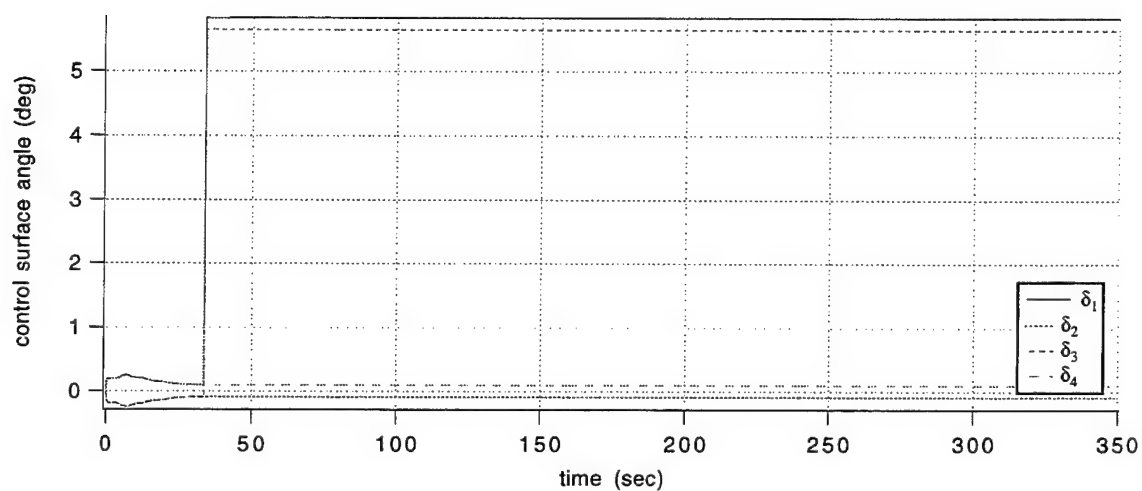Figure 26: Partially closed-loop range extension, aerodynamic angle of attack.

Figure 27: Partially closed-loop range extension, control deflections.

Time histories of the projectile and control system state variables are plotted in Figures 28 through 34 for a fully closed loop tracking trajectory simulation. Initial conditions for the simulation shown in Figures 28 through 34 are as follows: $x = y = z = \phi = \psi = v = w = q = r = p_i = \theta_{ERRI} = \psi_{ERRI} = v_{fil} = w_{fil} = 0$, $u = u_{fil} = 2788$ fps, $\theta = 45°$, $p = 31$ r/s. The fully closed loop simulations use an automatic flight control system that utilizes sensors which feedback the signals $x, y, z, \dot{x}, \dot{y}, \dot{z}, \psi, \theta, \phi, p, q$, and r (full state feedback) to guide the projectile onto a prespecified desired trajectory. The desired trajectory is specified in advance by a set of way points. Figure 28 plots range, altitude, and cross range for case 1 of the fully closed loop tracking simulation. In Figure 28, the dotted trace represents the commanded position, while the solid line represents the projectile position. The desired trajectory represents a range extension from 21.06 km to 34.9 km. This range extension is significantly less than the partially closed loop case shown previously. From the range time history, it is shown that the projectile flight control system is able to track the desired trajectory to attain a moderate extension in range. Around the apex of flight, the projectile does not track the desired path particularly well, and it is believed that this is due to the sharp gradients in the desired path and the reduction in control power that occurs at high altitude. Figure 28 also shows altitude vs. time and shows that the time of flight increases from approximately 79 s in the uncontrolled case to 133 s in the closed-loop case. Recall that for the partially closed loop case the overall time of flight was 351 s. The lateral range vs. time plot in Figure 28 shows that the lateral range is regulated within ±5 m. In contrast to the partially closed loop case, lateral range is small, since the projectile flight control system commanded cross range to zero ($y_c = 0$) at all times.

Figure 29 shows the body attitudes for the closed loop trajectory simulation. From the roll angle trace, it is seen that the roll channel control system eliminates the projectile roll rate and roll angle within 10 s. Also in Figure 29 the pitch attitude of the projectile is shown. Unlike an uncontrolled projectile where pitch attitude decreases monotonically, the pitch attitude decreases from an initial attitude of 45° and begins to oscillate at $t = 40$ s. The oscillation in pitch attitude is caused by the projectile maneuvering to track the desired trajectory. Figure 29 also plots yaw attitude vs. time, and it is shown that yaw attitude remains small throughout the time of flight. This is in contrast to the partially closed loop case where yaw angle was unregulated and monotonically increased due to a small persistent yaw rate. Figure 30 shows the three components of the body velocity vector for case 1 of the closed loop tracking simulation. From the range time history in Figure 28, it is seen that the terminal point ($z = 0$) occurs at a time of 133 s, which corresponds to a terminal velocity in Figure 30 of 235.3 m/s. While the moderate range extension profile reduces the terminal velocity by 24%, the decrease in terminal velocity is far less than the partially closed loop case shown earlier. The side velocity time history in Figure 30 is small throughout the time of flight except for some high-frequency transient oscillations at launch. The body vertical velocity shown in Figure 30 attains a maximum value of 27 m/s during maneuvering. As in the partially closed loop simulation, the vertical velocity is due to pitch commands that purposefully cause an angle of attack on the projectile, which, in turn, dictates that the relative velocity have nonzero components off the projectile axis of symmetry.

Figure 31 plots the three components of the body angular velocity vector for case 1 of the closed loop tracking simulation. It is seen from the roll rate time history that the action of the canards is to rapidly eliminate the roll rate from 31 rad/s to 0 within 10 s. Pitch rate is also plotted in Figure 31, and it shows oscillations between +2 and -5°/s, which are necessary for maneuvering. Yaw rate is shown in Figure 31 and, unlike the partially closed loop case, yaw rate settles to zero. Figure 32 plots the flight control system state variables p_I, θ_{ERRI}, ψ_{ERRI}. Figure 33 plots the projectile body angle of attack, projectile body aerodynamic forces, and projectile body aerodynamic moments. From the angle of attack time history in Figure 33, it is seen that the maximum body angle of attack is 6.63°, which is a relatively low angle of attack, indicating that the desired trajectory did not exceed the maneuver limits of the canard controlled projectile. Figure 34 plots the canard control surface deflection angles, and the total canard forces and moments. Comparing the projectile body aerodynamic forces with the total forces generated by the canards, it is seen that both the canards and the projectile body contribute vertical forces, which are used to keep the projectile aloft longer, hence extending range. In Figure 34, the canard deflection angle chart shows the deflections to be within ±3°, which is well within the imposed limits of ±10°. To zero roll rate and roll angle, canards 2 and 3 deflect identically while canards 1 and 4 also deflect identically, but in the opposite direction as canards 2 and 3. Since canards 1 and 3 are in the pitch plane of the projectile and effect pitch maneuvers, they are deflected by the pitch command ± the canard deflection to null roll rate. A nonzero canard deflection is necessary to null roll rate in the steady state because the aft fins on the projectile have an effective cant of 0.29°.

Figures 28 through 34 show that the trajectory of a canard-controlled projectile can be significantly altered from the baseline uncontrolled projectile in a predetermined manner. The prespecified command trajectory represented a moderate range extension profile, and the projectile tracked the desired trajectory well, particularly in the terminal portion of flight. Thus, actively controlled canards provide a suitable method for increasing artillery projectile accuracy. The simulation also shows that for a moderate range extension profile, the time of flight increases and the terminal velocity decreases but not as much as in the partially closed loop case where dramatic range extension was realized. This reaffirms the notion that any increase in range with canard control will come at the expense of time of flight and terminal velocity of the round.
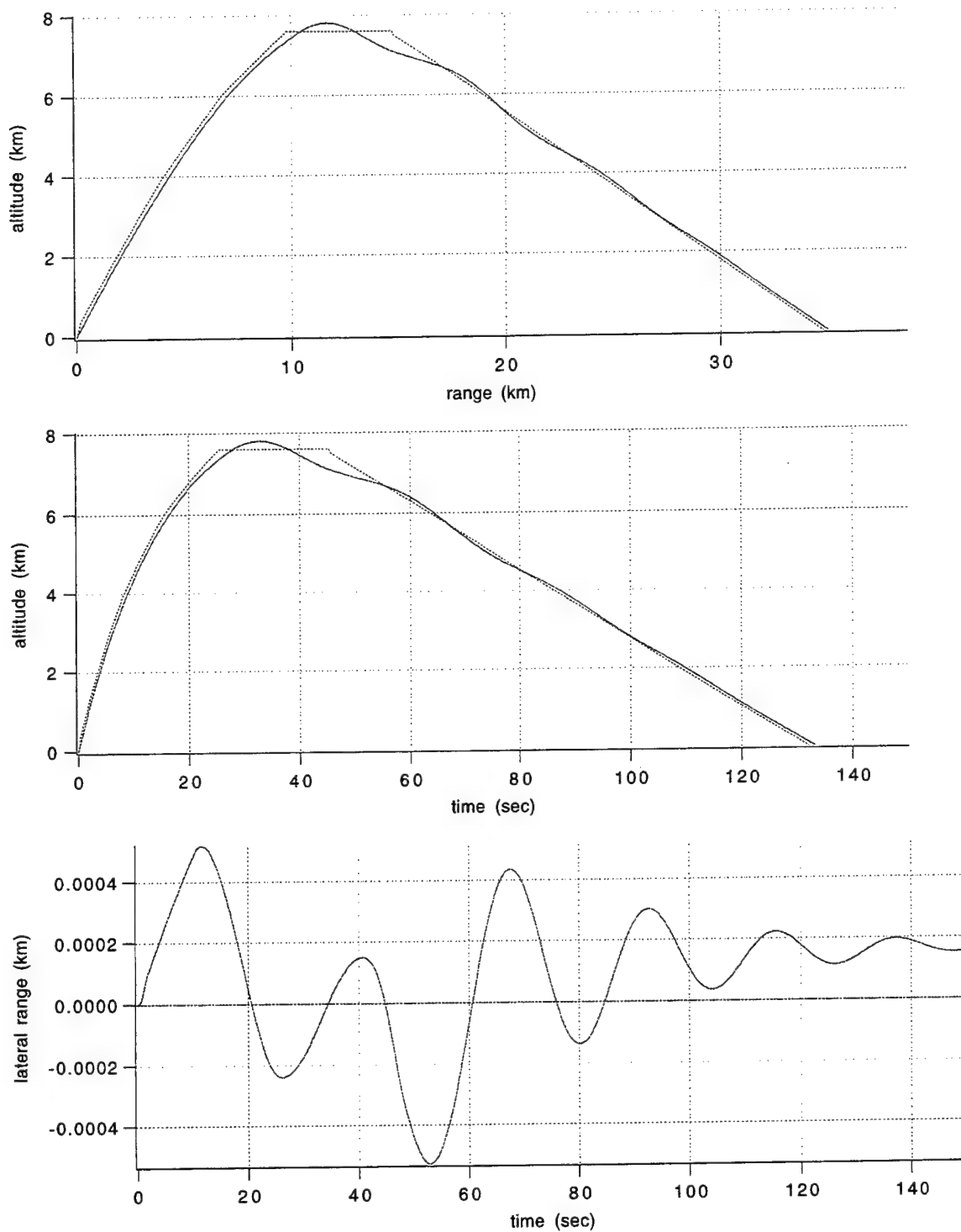
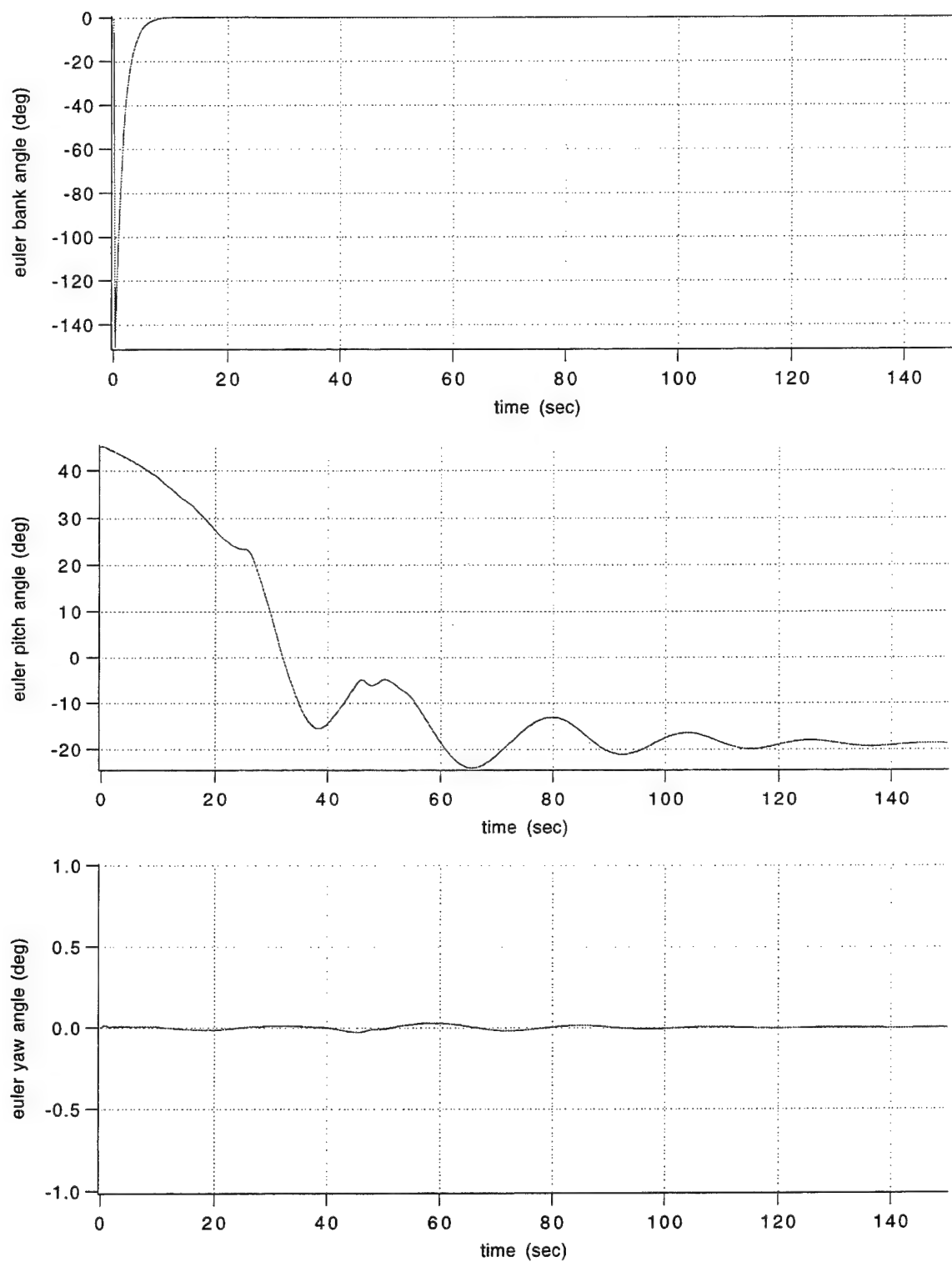Figure 28: Closed-loop tracking 1, position (solid = actual, dotted = commanded).

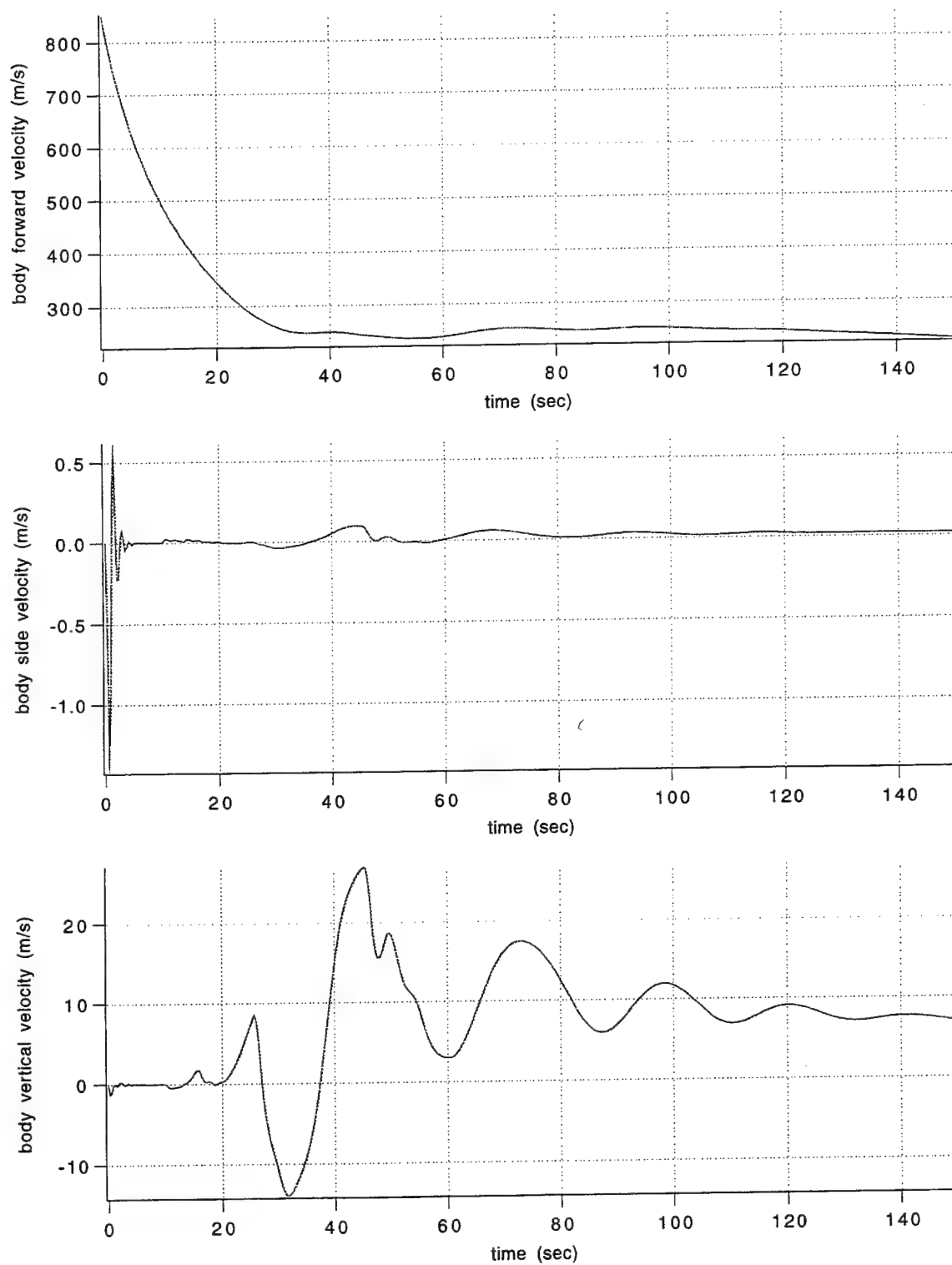Figure 29: Closed-loop tracking 1, Euler angles.

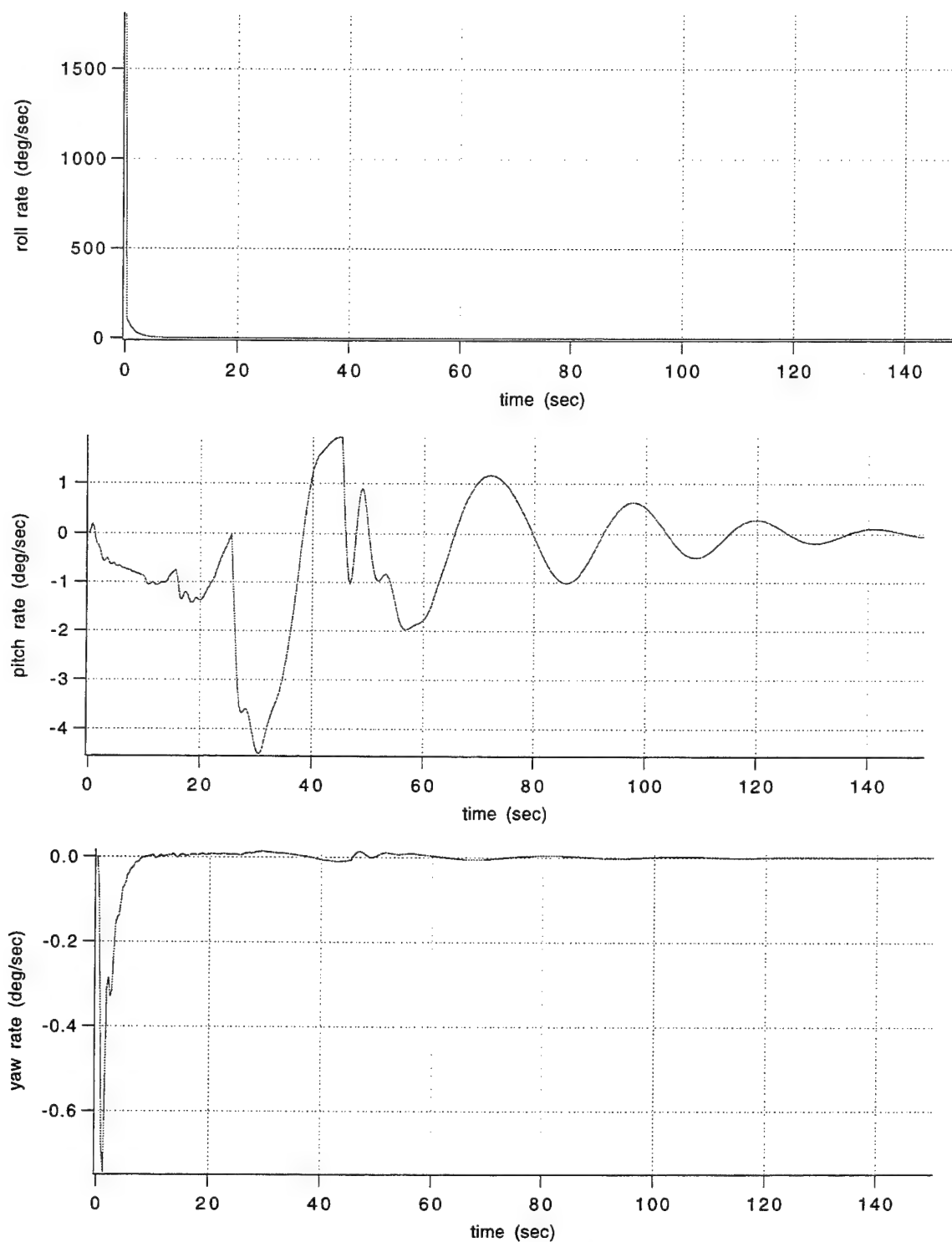Figure 30: Closed-loop tracking 1, body velocity.

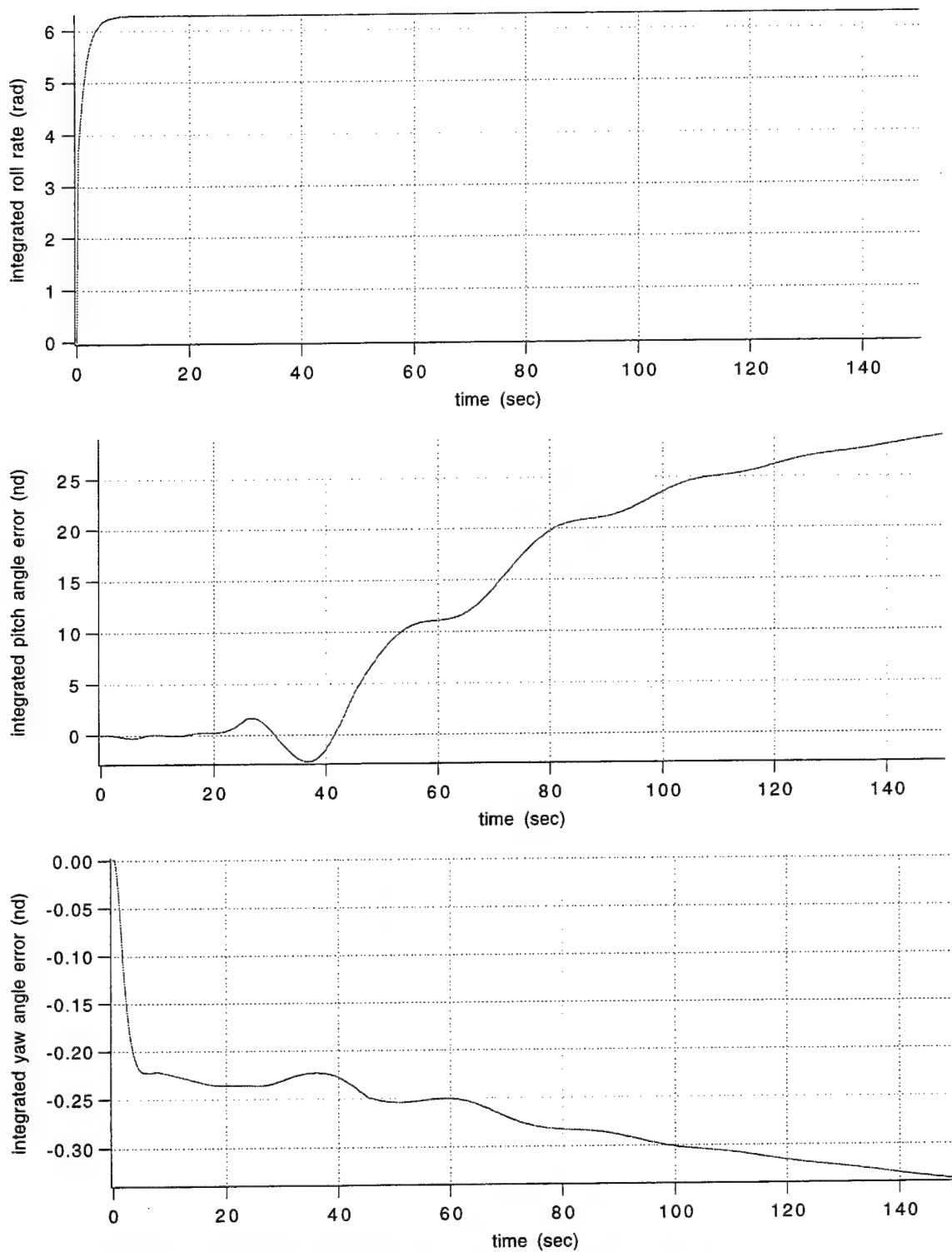Figure 31: Closed-loop tracking 1, body angular velocity.

Figure 32: Closed-loop tracking 1, integrated roll rate, theta error, and psi error.
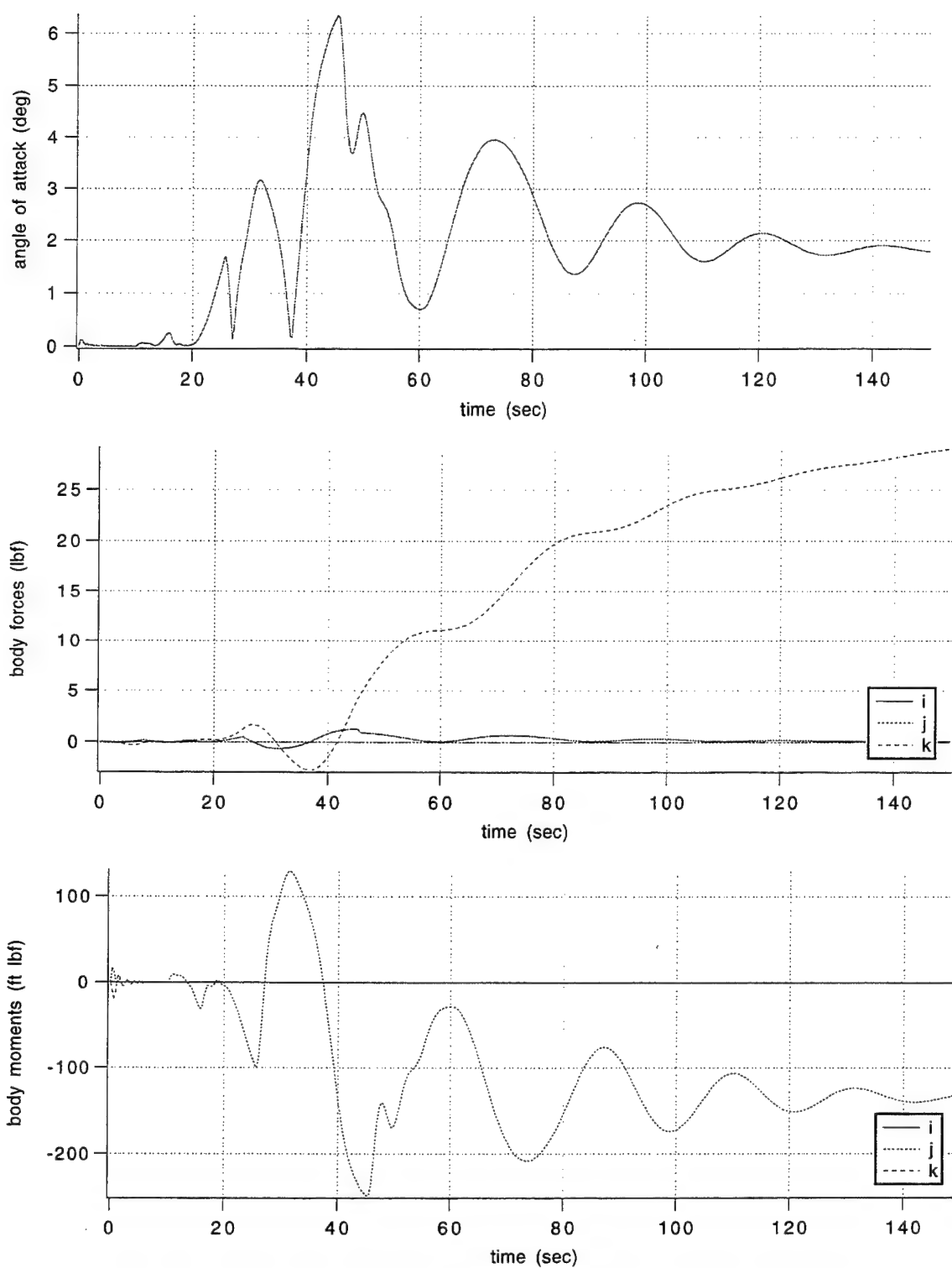
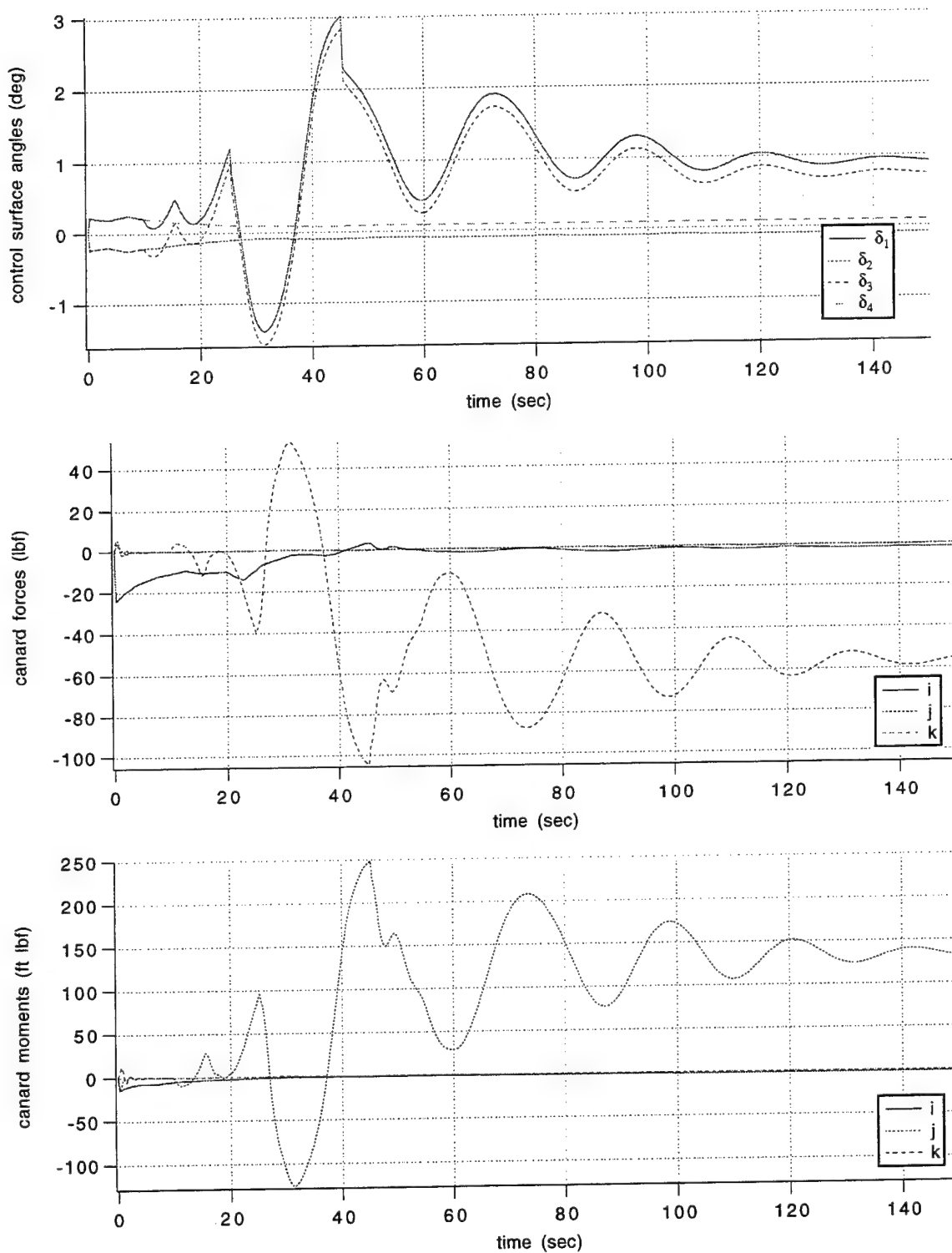Figure 33: Closed-loop tracking 1, angle of attack, body forces and moments.

Figure 34: Closed-loop tracking 1, controls, canards forces and moments.

35

Time histories of the projectile and control system state variables are plotted in Figures 35 through 41 for a fully closed loop tracking trajectory simulation. Initial conditions for the simulation shown in Figures 35 through 41 are as follows: $x = y = z = \phi = \psi = v = w = q = r = p_i = \theta_{ERRI} = \psi_{ERRI} = v_{fil} = w_{fil} = 0$, $u = u_{fil} = 2788$ fps, $\theta = 45°$, $p = 31$ r/s. The fully closed loop simulations use an automatic flight control system that utilizes sensors which feedback the signals $x, y, z, \dot{x}, \dot{y}, \dot{z}, \psi, \theta, \phi, p, q$, and r (full state feedback) to guide the projectile onto a prespecified desired trajectory. The desired trajectory is specified in advance by a set of way points. Figure 35 plots the range, altitude, and cross range for case 2 of the fully closed loop tracking simulation. In Figure 35, the dotted trace represents the commanded position, while the solid line represents the projectile position. The desired trajectory commands the projectile to a terminal range equal to the uncontrolled range, however, the projectile approaches the target from the opposite direction of fire. Thus, the projectile passes the desired target and subsequently returns to the target to attack the target from the rear in the terminal portion of the flight. The simulation results shown in Figures 35 through 41 represent a dramatically altered projectile trajectory. From the range time history in Figure 35, it is shown that the projectile flight control system is able to track the desired trajectory fairly well, at least as well as in the first closed loop simulation set, except in the area from 100 to 140 s into the flight.

From Equation 12, it can be seen that the $\dot{\psi}$ and $\dot{\phi}$ differential equations are singular when the Euler pitch attitude is 90°. When the $\dot{\psi}$ differential equation is singular, erroneous large projectile yaw attitudes are computed, which, in turn, generate erroneous large projectile angles of attack that create large erroneous aerodynamic forces and moments. While the simulation will run on the computer, the results are incorrect. In the case of the controlled projectile, matters are even worse, because the automatic flight control system uses yaw attitude to compute the canard deflection angles, so the pitch and yaw commands are erroneously large as well. For simulation set 2, shown in Figures 35 through 41, the Euler pitch attitude must go through 90°, since the desired trajectory has an infinite gradient in the pitch plane. In the simulation results this occurs at approximately $t = 100$ s and the results can be seen throughout all the state variables plotted in Figures 35 through 41. This problem is only due to the method of simulation and does not represent an inherent problem with the automatic flight control system, since in an implemented flight control system, the yaw angle signal would be generated from a sensor measuring the actual value and not a simulation. Further studies of desired trajectories which will force the projectile to attain a 90° pitch attitude will need to be simulated in another manner that does not entail a singularity at $\theta = 90°$. Such a simulation is possible by using quaternions to define the attitude of the projectile.
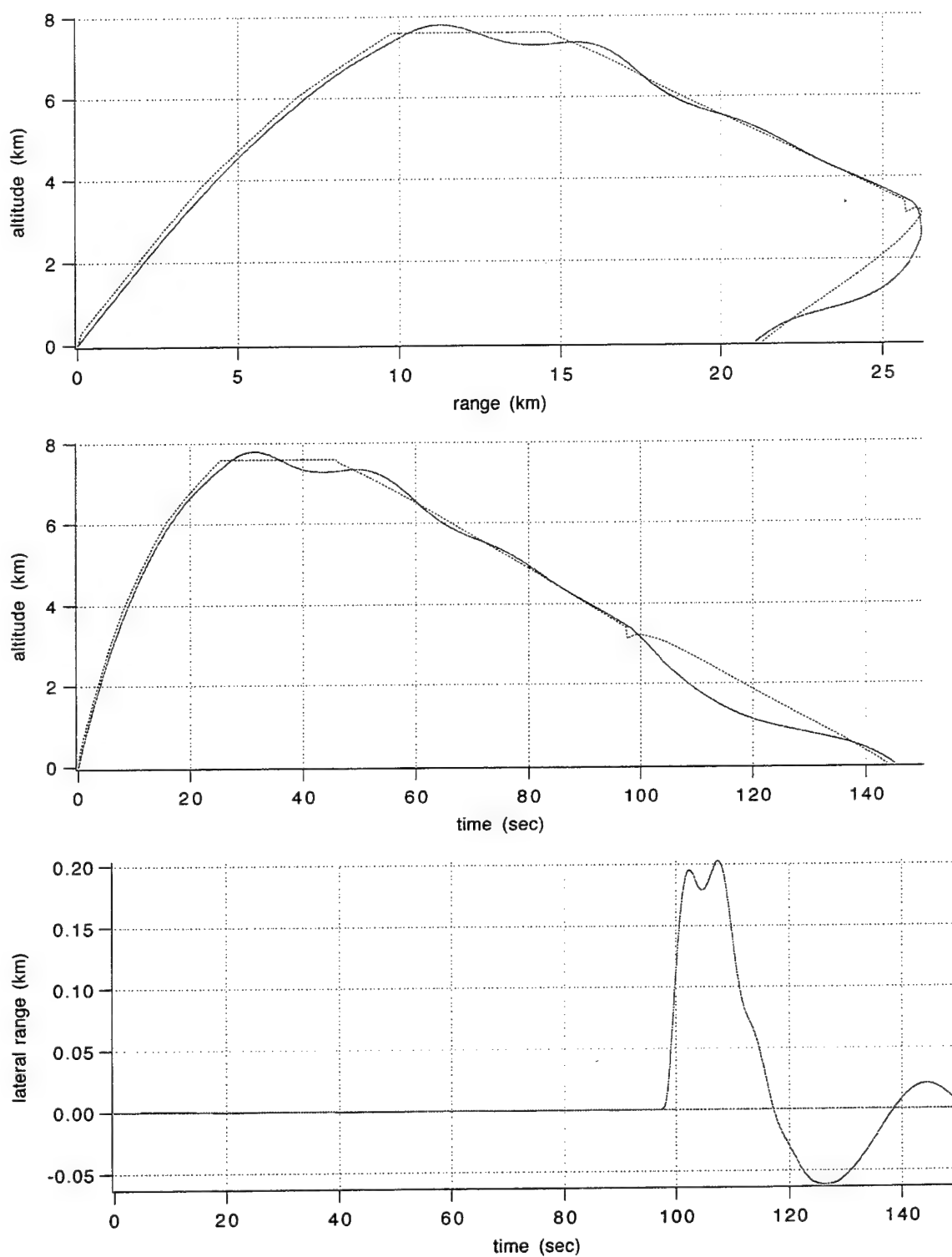
Figure 35: Closed-loop tracking 2, position (solid = actual, dotted = commanded).

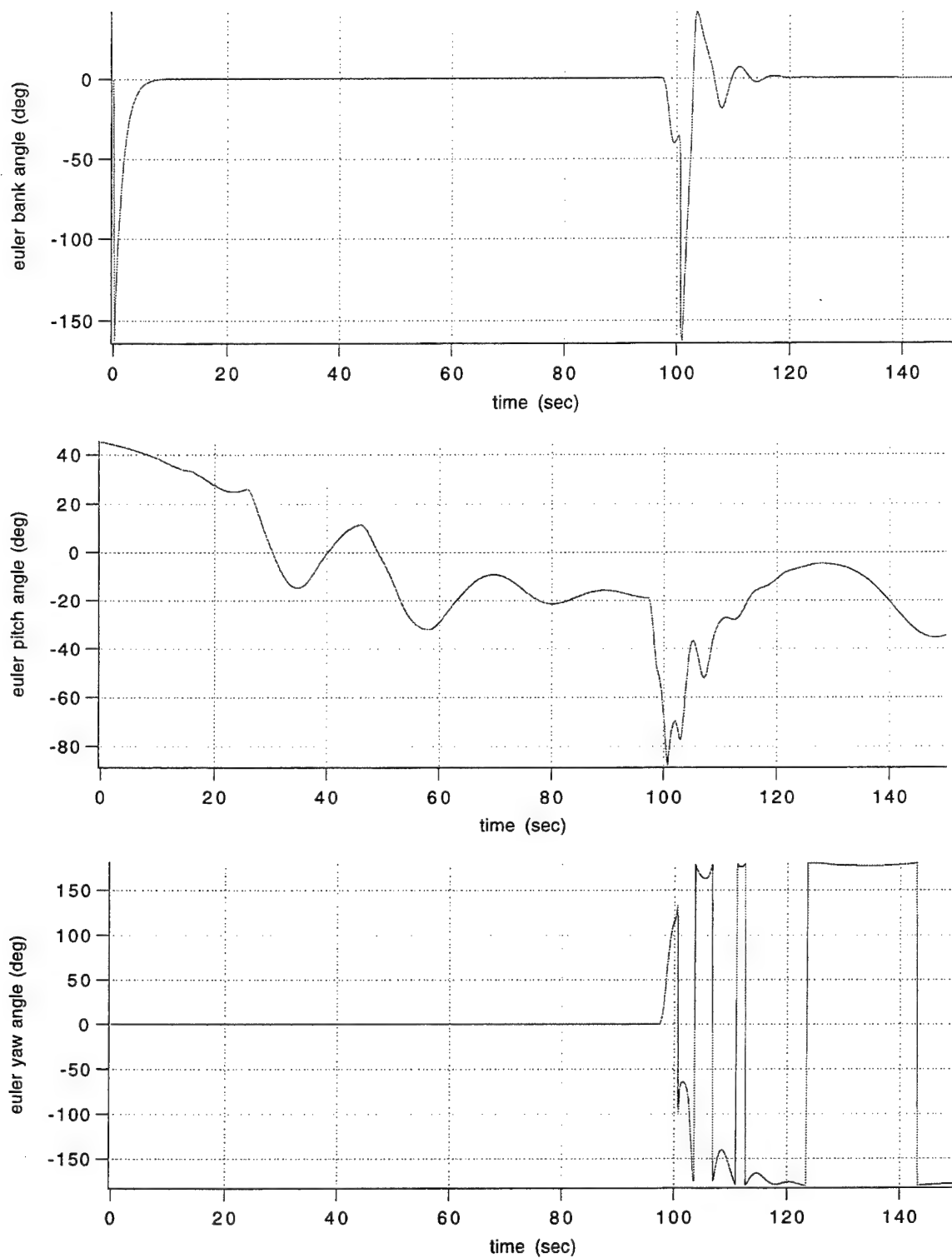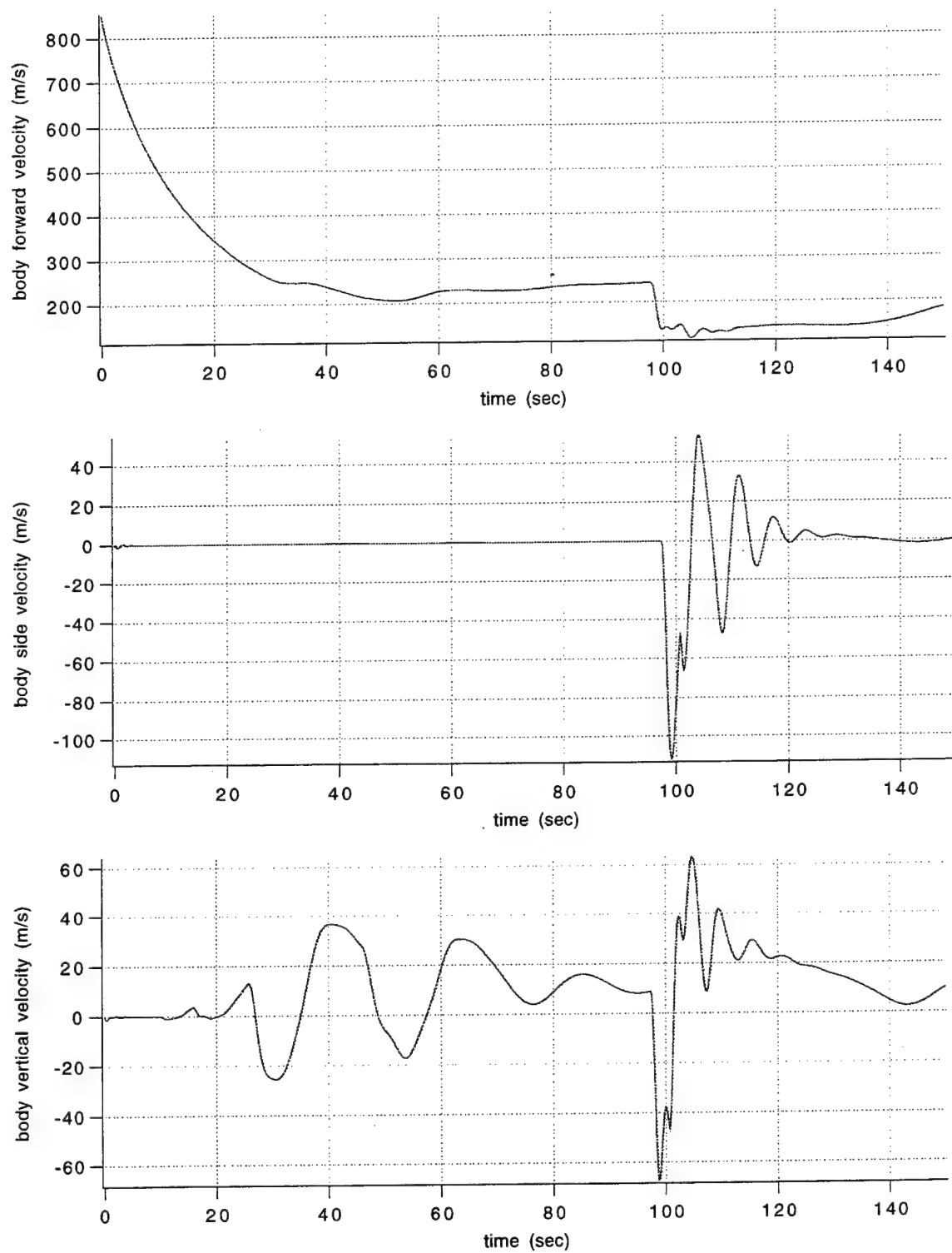Figure 36: Closed-loop tracking 2, Euler angles.

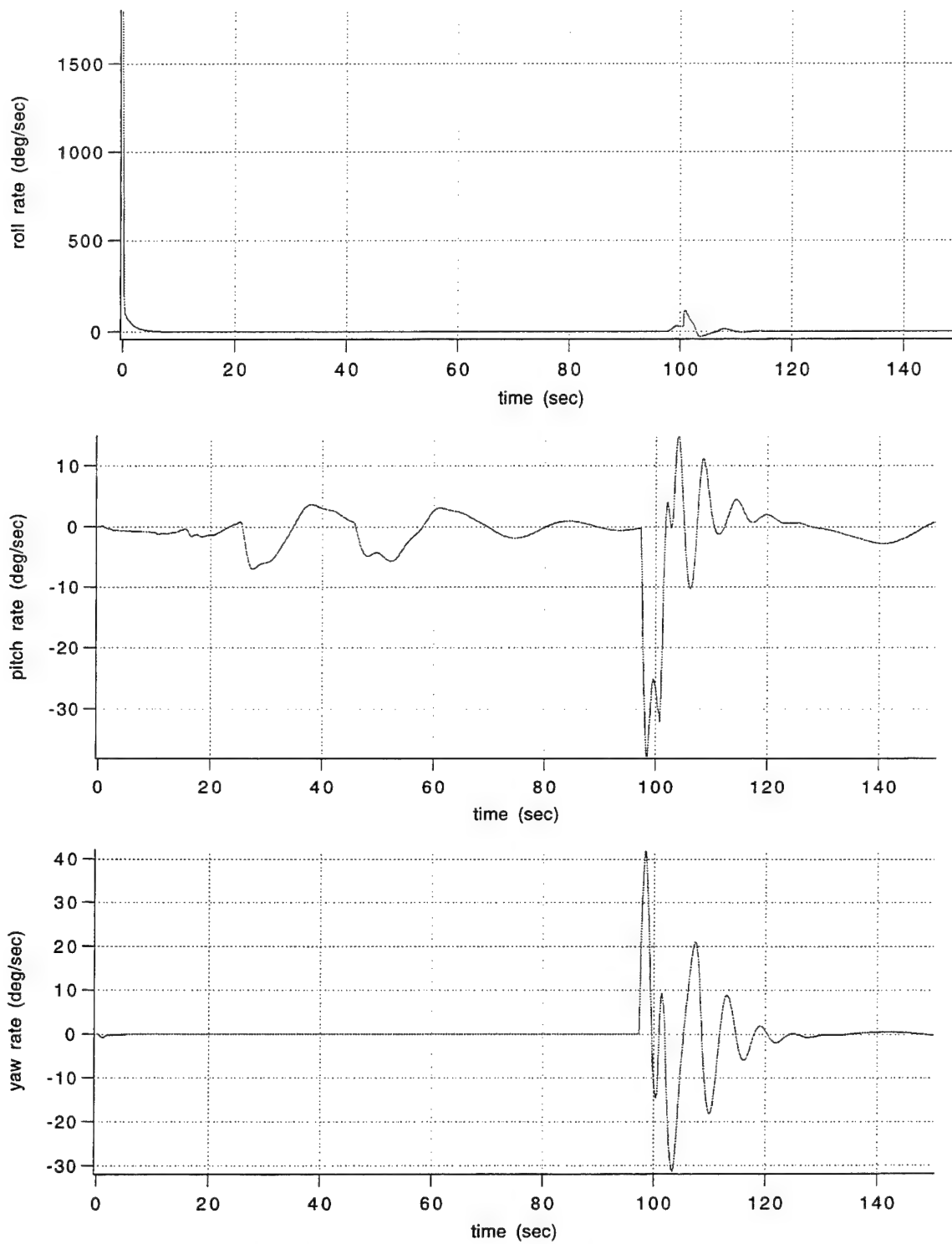Figure 37: Closed-loop tracking 2, body velocity.

39

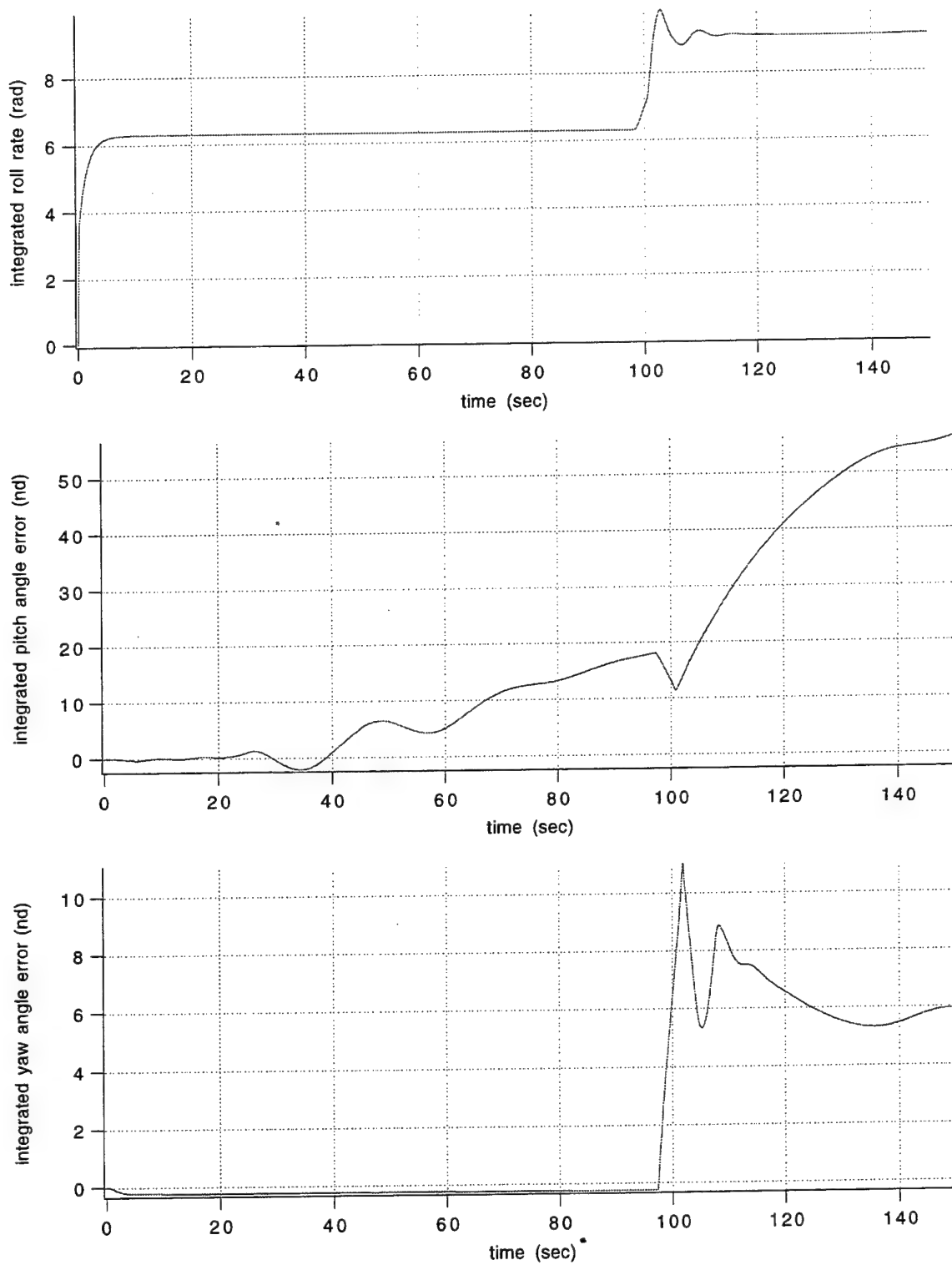Figure 38: Closed-loop tracking 2, body angular velocity.

Figure 39: Closed-loop tracking 2, integrated roll rate, theta error, and psi error.
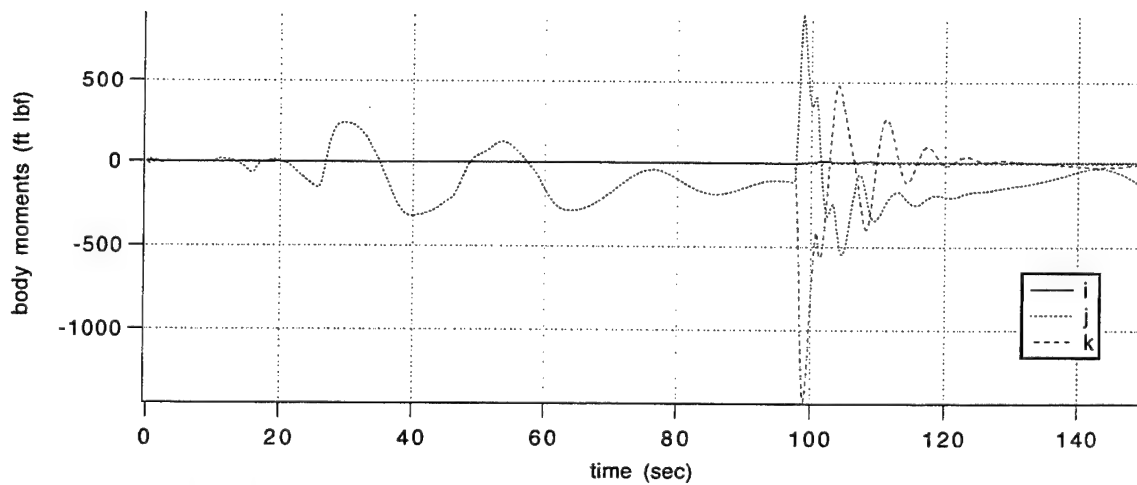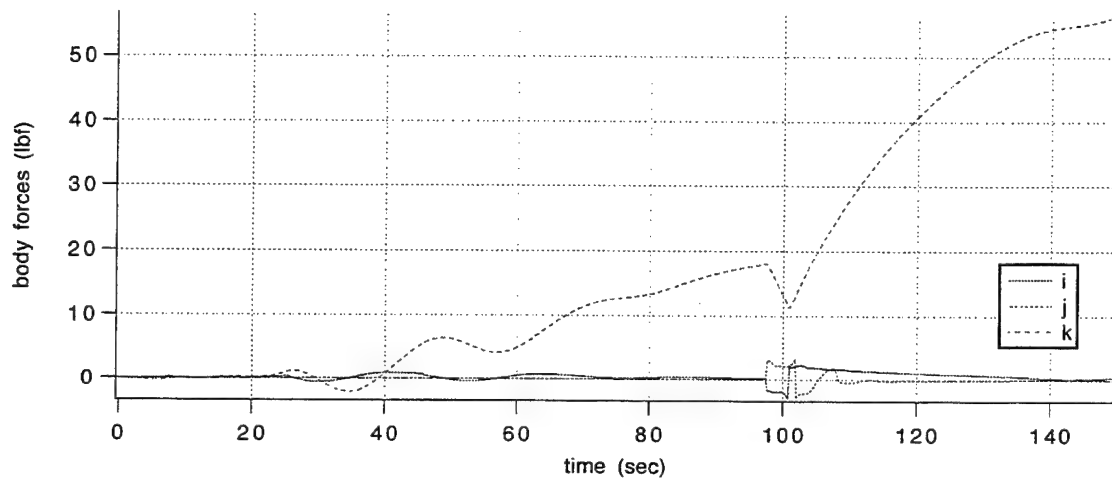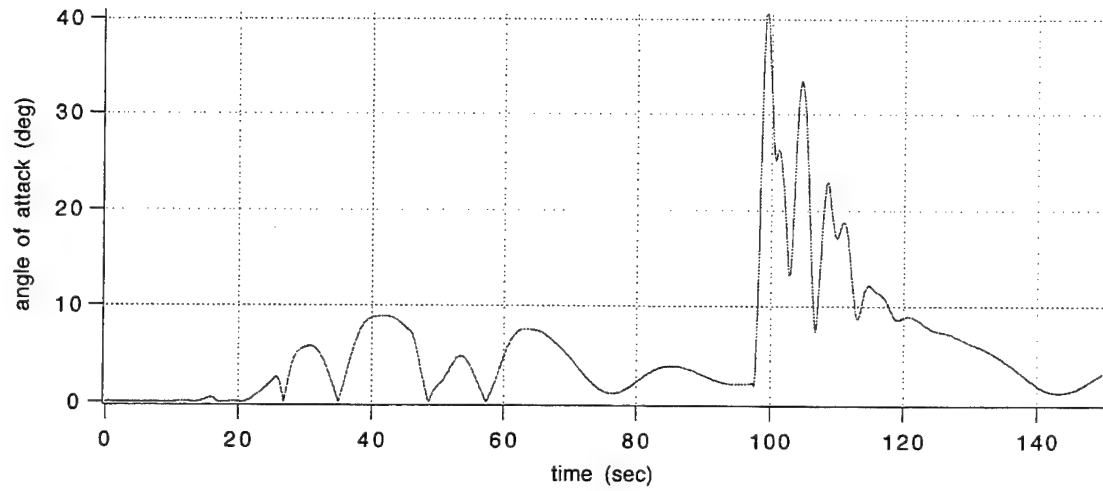
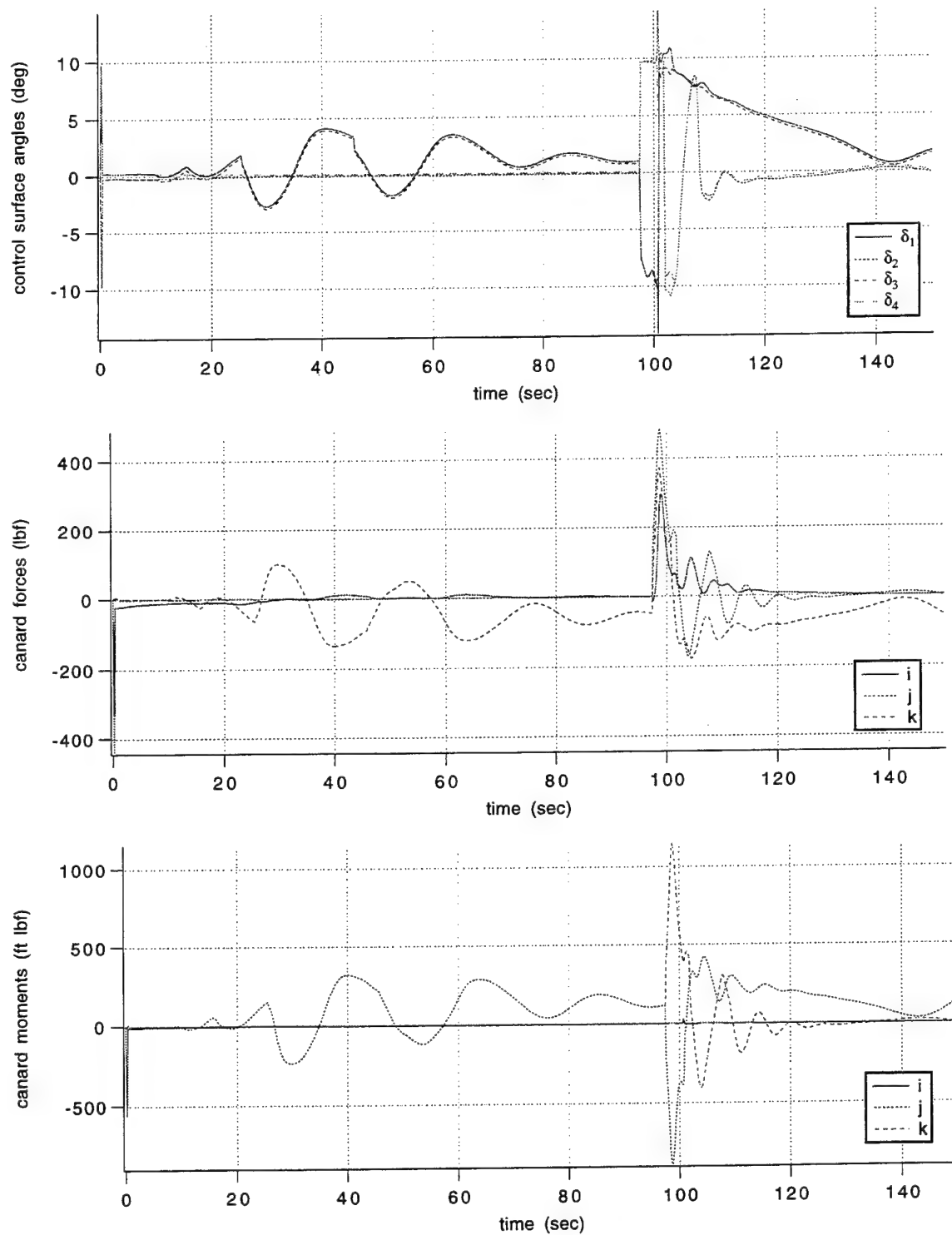Figure 40: Closed-loop tracking 2, angle of attack, body forces and moments.

Figure 41: Closed-loop tracking 2, controls, canards forces and moments.

4   Summary.

A mathematical model of a controllable artillery projectile has been developed and coded in FORTRAN. The projectile is modeled as a rigid body possessing six degrees of freedom. Aerodynamic forces and moments of the projectile body and canard lifting surfaces are a function of both angle of attack and local Mach number. A modified standard atmosphere is used for modeling air density and the speed of sound. By numerically integrating the equations of motion, trajectories can be generated for an unguided projectile, for a partially closed loop projectile (roll channel closed) with open loop pitch and yaw commands, or for a fully closed loop projectile system. In the fully closed loop configuration, a projectile automatic flight control system is used to first generate a desired trajectory and second to command the controllable canard lifting surfaces in such a way as to follow the desired path. The control system uses inertial position and velocity, roll rate, and attitude feedback to track an inertial position trajectory using the movable canard lifting surfaces. Besides time simulation, the computer code can also generate linear dynamic models of the projectile system at prespecified time points along the trajectory. The software was verified by comparing code results to hand calculation results from a single time step. The model has not been validated against range or firing table data.

The model was exercised in prediction of the response of an advanced projectile currently under development. For the projectile used in this study, it is shown that the range can be extended by 148% by commanding a full authority pitch maneuver at the trajectory's maximum altitude. While the canard projectile configuration can significantly increase range, it also has a large increase in overall time of flight from approximately 79 to 351 s. Another outcome of extending range is a significant reduction in impact velocity from approximately 309.6 to 105.7 m/s.

From closed loop simulation set 1, it was shown that the projectile automatic flight control system was capable of tracking a moderate range extension trajectory profile well, particularly in the terminal portion of the trajectory profile. Since the projectile tracked the desired trajectory well, impact point errors can be eliminated using a fully closed loop projectile control system. From closed loop simulation set 2, it was established that the current simulation technique has problems when the Euler pitch attitude goes through 90° due to a singularity in the equations of motion. It is recommended that the simulation be modified to use quaternion parameters to define the orientation of the body.

5 References.

1. Smith, J., Smith, K., Topliffe, R., "Feasibility Study for Application of Modular Guidance and Control Units to Existing ICM Projectiles." Contractor Report ARLCD-CR-79001, U.S. Army Armament, Research, and Development Command, Dover, NJ, 1978.

2. Von Mises, R. Theory of Flight. New York: Dover Publications Inc., 1959.

3. Etkin, B. Dynamics of Atmospheric Flight. New York: John Wiley and Sons, 1972.

4. Murphy, C. "Free Flight of Symmetric Missiles." BRL Report 1216, U.S. Army Ballistic Research Laboratory, Aberdeen Proving Ground, MD, 1963.

Intentionally left blank

NO. OF
COPIES   ORGANIZATION

2   DEFENSE TECHNICAL INFO CTR
           ATTN DTIC DDA
           8725 JOHN J KINGMAN RD
           STE 0944
           FT BELVOIR VA 22060-6218

1   HQDA
           DAMO FDQ
           ATTN DENNIS SCHMIDT
           400 ARMY PENTAGON
           WASHINGTON DC 20310-0460

1   US MILITARY ACADEMY
           MATH SCI CTR OF EXCELLENCE
           DEPT OF MATHEMATICAL SCI
           ATTN MDN A MAJ DON ENGEN
           THAYER HALL
           WEST POINT NY 10996-1786

1   DIRECTOR
           US ARMY RESEARCH LAB
           ATTN AMSRL CS AL TP
           2800 POWDER MILL RD
           ADELPHI MD 20783-1145

1   DIRECTOR
           US ARMY RESEARCH LAB
           ATTN AMSRL CS AL TA
           2800 POWDER MILL RD
           ADELPHI MD 20783-1145

3   DIRECTOR
           US ARMY RESEARCH LAB
           ATTN AMSRL CI LL
           2800 POWDER MILL RD
           ADELPHI MD 20783-1145

           ABERDEEN PROVING GROUND

2   DIR USARL
           ATTN AMSRL CI LP (305)

47

NO. OF COPIES	ORGANIZATION

1   HQDA
ATTN SARD TT
DR F MILTON
WASHINGTON DC 20310-0103

1   HQDA
ATTN SARD TT
DR F MILTON
WASHINGTON DC 20310-0103

15   COMMANDER
US ARMY ARDEC
ATTN AMSTA AR CCH
J DELORENZO
E FENNELL
P CHRISTAN
S MUSALI
B KONRAD
F RENNER
R SAYER
P DONADIO
R CARR
K FEHSAL
S GHASI
E LOGSDON
T LOUZERIO
M PALATHINGAL
C LEVECHIA
PICATINNY ARSENAL NJ
07806-5000

2   COMMANDER
US ARMY ARDEC
ATTN AMSTA AR AET A
J GRAU
C NG
PICATINNY ARSENAL NJ
07806-5000

1   COMMANDER
US ARMY ARDEC
ATTN AMSTA AR FSF GD
K PFLEGER
PICATINNY ARSENAL NJ
07806-5000

1   COMMANDER
USA YUMA PROV GRND
ATTN STEYT MTW
YUMA AZ 85365-9103

5   COMMANDER
US ARMY ARDEC
ATTN AMSTA AR FSF BV
V GALGANO
C GONZALES
C LANGEN
E DELCOCO
C CORDING
PICATINNY ARSENAL NJ
07806-5000

10   COMMANDER
US ARMY TANK MAIN
ARMAMENT SYSTEMS
ATTN AMCPM TMA
D GUZIEWICZ
R KOWALSKI
R DARCEY
R BROWN
R BILLINGTON
MAJ J WILSON
C KIMKER
R JOINSON
A HYDER
E KOPOAC
PICATINNY ARSENAL NJ
07806-5000

10   COMMANDER
US ARMY TACOM
ATTN AMCPEO HFM
AMCPEO HFM F
AMCPEO HFM C
AMCPM ABMS
AMCPM BLOCKIII
AMSTA CF
AMSTA Z
AMSTA ZD
AMCPM ABMS S W
DR PATTISON
A HAVERILLA
WARREN MI 48397-5000

1   COMMANDER
US ARMY TACOM
ATTN SFAE ASM AB SW
M KAHN
WARREN MI 48397-5000

49

2   ARROW TECH ASSOC INC
        ATTN R WHYTE
        W HATHAWAY
        PO BOX 4218
        SOUTH BURLINGTON VT
        05401-0042

1   CDR, USAARDEC
        ATTN: SMCAR-FSF-T,
                    J. WHITESIDE (BLDG 120)

ABERDEEN PROVING GROUND

38   DIR, USARL
        ATTN: AMSRL-WM,
                    I. MAY
                AMSRL-WM-W, C. MURPHY
                AMSRL-WM-WB,
                    F. BRANDON
                    G. BROWN
                    W. DAMICO
                AMSRL-WM-T, W. F. MORRISON
                AMSRL-WM-TC
                    W. DE ROSSET
                    R. COATES
                AMSRL-WM-P, A. HORST
                AMSRL-WM-PA, T. MINOR
                AMSRL-WM-PB,
                    P. PLOSTINS (10 CP)
                    M. BUNDY
                    A. MIKHAIL
                    K. SOENCKSEN
                    D. WEBB
                    D. SAVICK
                    B. GUIDOS
                    V. OSKAY
                AMSRL-WM-PC, B. FORCH
                AMSRL-WM-PD,
                    T. ERLINE
                    B. BURNS
                    L. BURTON
                    R. KASTE
                    S. WILKERSON
                    W. DRYSDALE
                    A. FRYDMAN
                    T. LI
                AMSRL HR M, G. L. HORLEY

REPORT DOCUMENTATION PAGE

Form Approved
OMB No. 0704-0188

Public reporting burden for this collection of information is estimated to average 1 hour per response, including the time for reviewing instructions, searching existing data sources, gathering and maintaining the data needed, and completing and reviewing the collection of information. Send comments regarding this burden estimate or any other aspect of this collection of information, including suggestions for reducing this burden, to Washington Headquarters Services, Directorate for Information Operations and Reports, 1215 Jefferson Davis Highway, Suite 1204, Arlington, VA 22202-4302, and to the Office of Management and Budget, Paperwork Reduction Project(0704-0188), Washington, DC 20503.

1. AGENCY USE ONLY *(Leave blank)*	2. REPORT DATE April 97	3. REPORT TYPE AND DATES COVERED Final, Jan 94 - Dec 95

4. TITLE AND SUBTITLE

Potential Field Artillery Projectile Improvements Using Movable Canards

5. FUNDING NUMBERS

PR: 1L162618AH80

6. AUTHOR(S)

Mark F. Costello

7. PERFORMING ORGANIZATION NAME(S) AND ADDRESS(ES)

U.S. Military Academy
ATTN: MADN-I
West Point, NY 10996

8. PERFORMING ORGANIZATION REPORT NUMBER

ARL-TR-1344

9. SPONSORING/MONITORING AGENCY NAMES(S) AND ADDRESS(ES)

U.S. Army Research Laboratory
ATTN: AMSRL-WT-PB
Aberdeen Proving Ground, MD 21005-5066

10. SPONSORING/MONITORING AGENCY REPORT NUMBER

11. SUPPLEMENTARY NOTES

12a. DISTRIBUTION/AVAILABILITY STATEMENT

Approved for public release; distribution is unlimited.

12b. DISTRIBUTION CODE

13. ABSTRACT *(Maximum 200 words)*

This report explores the possibility of actively controlling a projectile with four canard lifting surfaces, equally spaced radially, with the end goals of extending range, improving terminal accuracy, and shaping the trajectory of a projectile. A description of a general mathematical model used to predict the dynamic behavior of a canard-controlled projectile in atmospheric flight is given. The model is exercised in prediction of the response of an advanced projectile currently under development. For the projectile used in this study, it is shown that the maximum range can be extended by 148% using controlled canards. It is also shown that projectile trajectories can be shaped to follow a predetermined and significantly different path than the nominal trajectory.

14. SUBJECT TERMS

projectile dynamics, control, canards

15. NUMBER OF PAGES
55

16. PRICE CODE

17. SECURITY CLASSIFICATION OF REPORT	18. SECURITY CLASSIFICATION OF THIS PAGE	19. SECURITY CLASSIFICATION OF ABSTRACT	20. LIMITATION OF ABSTRACT
UNCLASSIFIED	UNCLASSIFIED	UNCLASSIFIED	SAR

NSN 7540-01-280-5500

Standard Form 298 (Rev. 2-89)
Prescribed by ANSI Std. 239-18   298-102

INTENTIONALLY LEFT BLANK.

USER EVALUATION SHEET/CHANGE OF ADDRESS

This Laboratory undertakes a continuing effort to improve the quality of the reports it publishes. Your comments/answers to the items/questions below will aid us in our efforts.

1. ARL Report Number/Author __ARL-TR-1344 (Costello [POC: Plostins])__ Date of Report __April 1997__

2. Date Report Received _____

3. Does this report satisfy a need? (Comment on purpose, related project, or other area of interest for which the report will be used.) _____

_____

_____

4. Specifically, how is the report being used? (Information source, design data, procedure, source of ideas, etc.) _____

_____

_____

5. Has the information in this report led to any quantitative savings as far as man-hours or dollars saved, operating costs avoided, or efficiencies achieved, etc? If so, please elaborate. _____

_____

_____

6. General Comments. What do you think should be changed to improve future reports? (Indicate changes to organization, technical content, format, etc.) _____

_____

_____

_____

CURRENT
ADDRESS

Organization
_____

Name _____ E-mail Name _____

Street or P.O. Box No.
_____

City, State, Zip Code

7. If indicating a Change of Address or Address Correction, please provide the Current or Correct address above and the Old or Incorrect address below.

OLD
ADDRESS

Organization
_____

Name
_____

Street or P.O. Box No.
_____

City, State, Zip Code

(Remove this sheet, fold as indicated, tape closed, and mail.)
(DO NOT STAPLE)